UNIVERSIDAD DE CONCEPCIÓN
FACULTAD DE CIENCIAS FÍSICAS Y MATEMÁTICAS

Mass spectrometry of silica nanoparticles for the study of surfaces of astrochemical interest

Por: Carolina Daniela Condeza Rodríguez

Tesis presentada a la Facultad de Ciencias Físicas y Matemáticas de la Universidad de Concepción para optar al grado académico de Magíster en Ciencias con Mención en Física

Julio 2026
Concepción, Chile

Profesor Guía: Pablo Solano Palma

A mi familia

AGRADECIMIENTOS

Quiero agradecer a mi familia, en especial a mis padres por apoyarme constantemente y dejarme estudiar algo que yo quería. A mi abuela por siempre desearme que tuviera un buen día antes de irme a la U. A mi hermana que me ha acompañado en cada momento de este proceso. A mi prima Javiera por motivarme a seguir adelante las veces que me desanimaba y pensaba en congelar o abandonar la carrera.

A mis amigas, por acompañarme a lo largo de todos estos años. A mi pareja Fernando, por su inmenso apoyo y por estar siempre ahí cuando lo necesito.

A mi profesor guía, Pablo Solano, por su paciencia y por siempre resolver nuestras dudas. También, al equipo de LAMP y de CODE por crear un ambiente bonito y agradable en el laboratorio, me siento muy agradecida de haber podido trabajar ahí.

Resumen

Simular las condiciones del medio interestelar (ISM) en un ambiente de laboratorio es relevante para comprender mejor los complejos procesos físicos y químicos que gobiernan la evolución del polvo cósmico. En este contexto, esta tesis detalla el desarrollo y caracterización de un montaje experimental diseñado para simular análogos de granos de polvo, atrapando nanopartículas de sílice (SiO_2) en un ambiente de alto vacío. Utilizando una trampa cuadrupolar de iones no destructiva, las nanopartículas fueron capturadas y su carga fue sistemáticamente modificada. Al monitorear las variaciones resultantes en las frecuencias seculares mediante la dispersión de la luz de la partícula, se determinó la razón entre su masa y su carga.

Se abordan además desafíos técnicos respecto a la aglomeración de nanopartículas y el método de inyección utilizado. Finalmente, se discuten las perspectivas futuras acerca de cómo lograr el objetivo de detectar y medir la adsorción y desorción de especies gaseosas en la superficie de la nanopartícula.

Keywords – Astroquímica, espectrometría de masas, granos de polvo.

Abstract

Simulating interstellar medium (ISM) conditions in a laboratory environment is relevant to better understand the complex physical and chemical processes that govern the evolution of cosmic dust. In this context, this thesis details the development and characterization of an experimental setup designed to simulate dust grain analogues by trapping silica (SiO_2) nanoparticles in a high-vacuum environment. Utilizing a non-destructive quadrupole ion trap, nanoparticles were captured and their charge was systematically modified. By monitoring the resulting shifts in secular frequencies through light scattering, the particle's mass to charge ratio was determined .

Technical challenges regarding the clumping of nanoparticles and the injection method used, are addressed. Finally, we discuss about future prospects on how to achieve the objective of detecting and measuring the adsorption and desorption of gas phase species on the surface of the nanoparticle.

Keywords – Astrochemistry, mass spectrometry, dust grains.

Contents

List of Figures

Symbols

a	Radius of a nanoparticle	m
a(BET)	BET area or specific surface area	m^2
C	BET constant	
c	Speed of light	m/s
D	Diffusivity	cm^2/s
E_1	Binding energy of the first monolayer	eV
E_{ads}	Adsorption energy	eV
E_b	Binding energy between a particle and a surface	eV
E_d	Desorption energy	eV
E_f	Electric field	V/m
E_L	Energy requiered for the gas to condense	eV
e	Charge	C
I_0	Intensity of the incident light	W/m^2
$\Delta\dot{h}$	Differential molar enthalpy	eV/mol
K	Langmuir constant	$torr^{-1}$
k_{ads}	Rate of adsorption	s^{-1}
k_B	Boltzmann constant	eV/K
k_{des}	Rate of thermal desorption	s^{-1}
k_H	Adsorption equilibrium constant (also known as Henry's constant)	
L	Avogadro number	mol^{-1}
m	Mass of a nanoparticle	g
m_i	Mass of the adsorbate	g
m_s	Mass of the solid's surface	g
N_a	Number of adsorbed particles	
N_s	Number of sites available for adsorption	
$\boldsymbol{n}$	Specific surface excess amount	mol/g
n_a	Adsorbed amount	mol
n_d	Number density of the dust grain	cm^{-3}
n_s	Surface density of the adsorbing sites	cm^{-2}
$\boldsymbol{n}_m$	Monolayer capacity	mol/g
P	Partial pressure of a specific gas species	torr
p	Equilibrium pressure (pressure just above the surface)	torr

p_0	Saturation vapour pressure	torr
S	Sticking coefficient	
s	Entropy	eV/K
T	Temperature of the surface	K
T_i	Temperature of the adsorbed species	K
V	Voltage of the trap	V
V_T	Total volume adsorbed	cm^3
V_M	Volume of a monolayer	cm^3
v_i	Velocity of the adsorbate	cm/s
z_m	Distance between two materials	m
z_R	Critical charge of the Rayleigh limit	C
Δ	Change in Fermi energy	eV
ε_0	Vacuum permittivity	$C^2N^{-1}m^{-2}$
γ	Surface tension	N/m
λ	Mean square jump distance	cm
ν_0	Vibrational frequency of the adsorbate	Hz
Ω	Frequency of the trap	Hz
ϕ	Potential energy	eV
ϕ_n	Work function	eV
φ	Surface concentration of species	mol/cm^2
σ	Area occupied by an adsorbate on the surface	cm^2
σ_d	Cross section of a dust grain	cm^2
θ	Surface coverage	

Chapter 1

Introduction

1.1 Astrochemistry

Astrochemistry is the study of the chemical composition of the universe and the reactions that give rise to the formation of diverse molecules. To date more than 250 molecules have been identified in interstellar clouds and circumstellar shells. Among several compounds we can also find the main functional groups that are needed to begin the formation of prebiotic molecules and RNA (Guélin & Cernicharo, 2022). Although plenty of the detected gas phase species are common on Earth, there are others which are considered exotic according to terrestrial standards (Herbst & Van Dishoeck, 2009). These molecules can be identified through their electronic, vibrational and rotational spectra. Typically, electronic transitions of simple molecules arise in the ultraviolet or visible range, vibrational bands lie in the infrared portion and rotational lines are found at radio wavelengths (Snow & McCall, 2006).

Interstellar matter is composed of molecular and atomic gas and dust grains (Yamamoto, 2017). Some of this material is found in regions known as interstellar clouds (Herbst, 2005), which are the birthplaces of stars and planets, and consist of gas and submicrometer-sized dust grains formed from refractory compounds assembled by gravity (Hama & Watanabe, 2013).

We can classify clouds as diffuse or dense. The former consist of regions where temperatures are lower than 80 K, with density of 10^2 molecules cm^{-3}, so the matter in these regions is relatively transparent, since light and radiation can

pass through them. On the other hand, we have dense clouds, which are more chemically relevant. These regions have temperatures around 10 K and typically contain 10^4 H_2 molecules cm^{-3}. Because of the low temperatures, the grains are covered with a layer of ice, a few Å thick (Hama & Watanabe, 2013; Herbst, 2005). In dense molecular clouds, dust grains tend to be negatively charged, because they typically have a large electron affinity, and the ionization occurs mainly by cosmic rays, as the grains are shielded from UV radiation. This can be contrasted with the diffuse cloud case, where dust is positively charged due to photoionization (Yamamoto, 2017).

Our knowledge of interstellar dust is based mostly on the interaction of the grains with electromagnetic radiation, i.e. absorption, emission and scattering (Draine, 2003b, 2009). Already by 1930, the presence of dust was deduced due to the reddening of starlight, because grains absorb and scatter shorter wavelengths (UV) more effectively than longer wavelengths (Vidali, 2013). Based on observations of ultraviolet extinction, scattering of visible light and polarization of starlight, it has been noted that the size distribution of the grains ranges from a radius of $\sim 0.03\,\mu$m to $\sim 1\,\mu$m (Klessen & Glover, 2014), with an average size of 0.1 μm.

Dust grains have a central role in the interstellar medium, from the thermodynamics and chemistry of the gas, to the dynamics of star formation. In contrast to gas-phase reactions, the grain surface can be a third body that absorbs the excess reaction energy. Therefore, reactions yielding only one product can proceed on the surface. An example of this is the hydrogen molecule; when 2 hydrogen atoms collide in the gas phase, a molecule tentatively forms but it is not stable because it can not discard energy unless it emits a photon or there is a third body (Yamamoto, 2017). Other relevant molecules such as H_2O, CO_2 and organic molecules require surface reactions to attain the observed abundances (Hama & Watanabe, 2013).

Regarding the composition of dust grains, it was discovered in 1977 that the average interstellar extinction could be satisfactorily reproduced by a grain model containing graphite and silicate grains (Draine, 2003a). The adsorption of gas-phase species on the surface leads to the formation of ice layers on the grains. The ice mantles are predominantly composed of H_2O in the amorphous phase, combined with other molecules such as CO, CO_2, NH_3, CH_4, H_2CO and CH_3OH (Hama & Watanabe, 2013). They can also contain polycyclic aromatic hydrocarbons

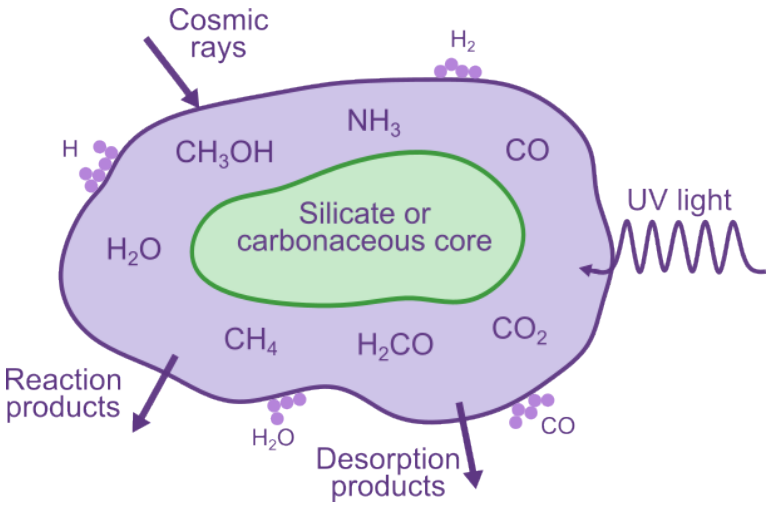

Figure 1.1.1: Typical illustration of a dust grain covered with ice layers, adapted from Fraser et al., 2002.

(PAHs), which are large carbon based molecules (Cuppen et al., 2017). When gas-phase species collide with the surface of solid water ice, they exhibit a distinct behavior mainly influenced by impact velocity, binding energy with the ice and energy barriers of reaction (Cui & Herbst, 2024). Figure 1.1.1 summarizes the main composition of dust grains and the reactions that occur on their surfaces.

It has been suggested that the origin of dust resides in asymptotic giant branch (AGB) stars and supernovae, nevertheless, this could account for only a fraction of the total grains present in the ISM, due to the destruction of dust caused by shock waves (Draine, 2009; Krasnokutski et al., 2014). Therefore, the observed abundance is attributed to the growth of material on already existing grains, which is known as depletion (Draine, 2009).

Silicate minerals have strong absorption resonances due to the Si-O stretching mode near 10 μm, at 18 μm due to the O-Si-O bending mode, and it seems certain that the interstellar 9.7 μm feature is also due to silicates (Henning, 2010). Although crystalline silicate minerals are found in cometary and circumstellar grains, they generally have sharp features that are not seen in the broad interstellar 10 μm feature, leading to the conclusion that interstellar silicates are mainly amorphous rather than crystalline (Draine, 2003b). Therefore, around 95% of the silicate material in the interstellar medium is amorphous (Draine, 2003a). These grains are found to be rich in magnesium and also contain iron, with an average stochiometry between pyroxene ($Mg_xFe_{(1-x)}SiO_3$, with x between 0 and 1) and

olivine ($Mg_{2x}Fe_{2(1-x)}SiO_4$, with x between 0 and 1) (Min et al., 2007), the latter being more prevalent, since it corresponds to around an 85% of the amorphous grains (Kemper et al., 2004). Although pure SiO_x grains have not been observed in the ISM, diatomic SiO has been detected and this compound is considered to be a precursor of the silicates found in molecular clouds (Studemund et al., 2025). Also, experiments have shown the formation of SiO at low temperatures (Krasnokutski et al., 2014).

Despite all the discoveries that have been made regarding the molecular composition of interstellar clouds, there are still many aspects of interstellar dust that remain uncertain. The challenge in the study of reactions of dust grain analogues reside in the lack of knowledge on actual cosmic dust and in the complexity of accurately reproducing their chemical composition in experiments (Vidali, 2013).

1.2 Goal and outline of the thesis

It is quite difficult to reproduce astronomical conditions in a laboratory setting (Burke & Brown, 2010; Potapov & McCoustra, 2021), since there are multiple variables to take into consideration, for example, one cannot replicate the timescales at which some processes occur, since they may take quite long, for instance accretion can take around $\sim 10^4$ yrs.

There have been done several experiments to study adsorption and desorption of species on surfaces under interstellar conditions (Burke & Brown, 2010; Dulieu et al., 2010; Linnartz et al., 2015; Noble et al., 2012), but most of these are performed on films of substrates such as gold or copper, which are then covered by ice layers. Although this is useful to gain insights about the formation of molecules on the surface of the ice, they do not necessarily take into account the actual morphology and chemical composition of the dust grains in the ISM, therefore there is still much unknown information about the reactions occurring in these regions (Wakelam et al., 2017). Some of the research that has been done around this topic considers that at high coverages, desorption of species is of zeroth order, hence the morphological features of the substrate are not relevant in the desorption process (Green et al., 2009).

However, more recent findings suggest that in addition to heating rate and grain

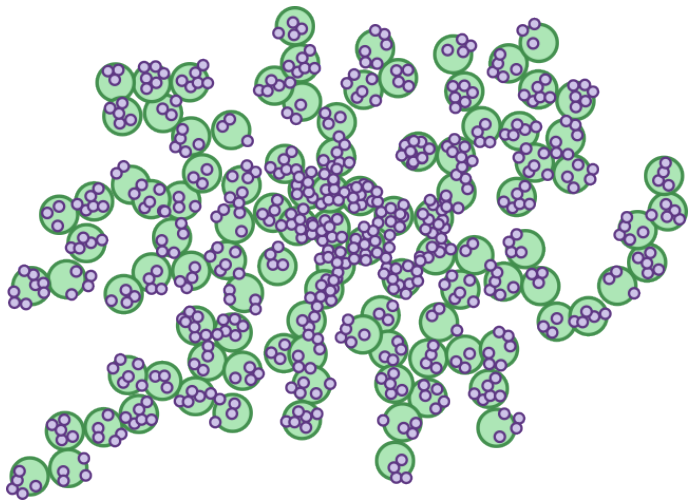

Figure 1.2.1: Sketch of dust grains (green) covered with ice molecules (purple), reproduced from Potapov et al., 2020.

size, surface type and its degree of cristallinity is an important factor for desorption in the sub-monolayer regime (Noble et al., 2012). It has been shown that binding energies will be different on the surface of a dust grain analogue compared to a large solid surface, and that the grain surface has a catalytic effect. Also, it has been proposed that instead of hundreds of monolayers, dust grains are only covered by a few layers of ice, hence the interaction with their surface would have a bigger role than it is often recognised (Potapov et al., 2020). Figure 1.2.1 shows an illustration of grains with ice on their surface.

Over the last three decades, research has been carried out around the characterization of SiO_2 nanoparticles in quadrupole ion traps (Esser et al., 2019; Schlemmer et al., 2004; Schlemmer et al., 1999, 2001), but these have not been oriented to the study of astrochemical processes. Therefore, the goal of this thesis is to measure the mass of a single trapped amorphous SiO_2 nanoparticle, so in the future we can study the adsorption of argon on its surface, which will be given by a change in the mass of the nanoparticle. This is done in the context of the COsmic Dust Experiment (CODE), that aims to recreate the conditions of the cold regions of the ISM and study the binding energies of different species on the surface of a cosmic dust analogue.

The thesis is separated as follows: the second chapter focuses on surface science concepts and methods we expect to apply on the experiment; the third chapter explains the theory behind quadrupole traps and mass spectrometry; chapter 3

shows the components of the experimental setup of CODE, along with the data acquisition process. Chapter 4 contains the results obtained and their analysis. Then, in chapter 5 is detailed what are our current limitations and what are the next steps to follow. Finally, the conclusion in chapter 6 reviews the work presented.

Chapter 2

Surface processes

2.1 Adsorption

When gas-phase species hit a surface, they can attach to it, and this process is known as adsoprtion. For species accreting on the surface of a grain, the rate of adsorption will be

$$k_{\text{ads}} = n_d \sigma_d \langle v_i \rangle S(T_i, T), \tag{2.1.1}$$

where n_d is the number density of dust, σ_d is the cross section of the grain, T_i and T are the temperature of the gas species and the grain respectively; $S(T_i, T)$ is the sticking coefficient, which is the probability of an atom adsorbing (i.e. an sticking coefficient of 1 means an atom will always adsorb upon reaching the surface). The mean speed of the molecule is $\langle v_i \rangle$, given by

$$\langle v_i \rangle = \sqrt{\frac{8 k_B T_i}{\pi m_i}}, \tag{2.1.2}$$

where m_i is the mass of the molecule (Tielens, 2013; Yamamoto, 2017).

The ratio between adsorbed particles N_a and the sites available for adsorption on the surface N_s is the surface coverage,

$$\theta = \frac{N_{\text{a}}}{N_{\text{s}}}.$$

When $\theta = 1$ we have a monolayer and when $\theta > 1$ we have multilayers. Figure 2.1.1 illustrates different types of surface coverage and also the formation of islands.

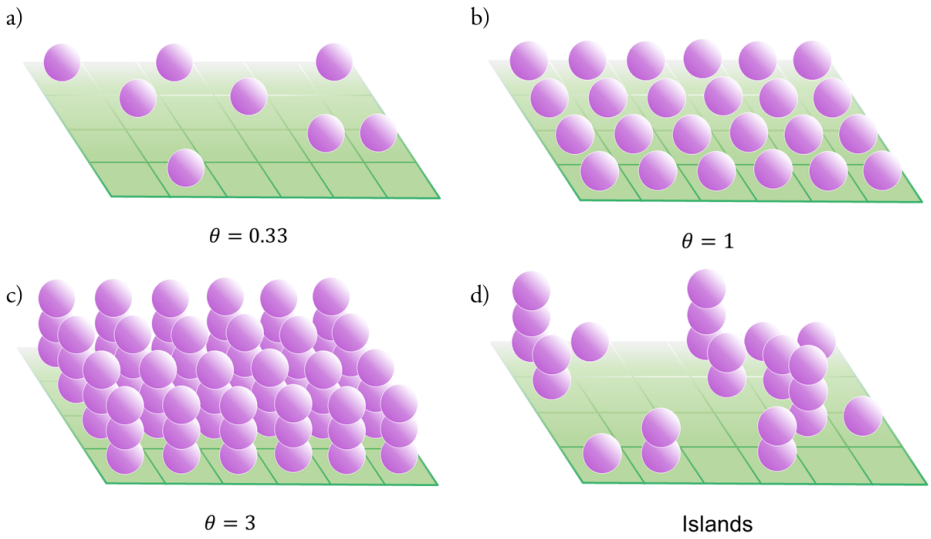

Figure 2.1.1: a) Submonolayer, b) monolayer and c) multilayer coverages. Image d) illustrates islands on the surface.

The release of an atom or molecule from a surface is known as desorption. The rate for thermal induced desorption is expressed as

$$k_{\text{des}} = \nu_0 \exp\left(-\frac{E_{\text{d}}}{k_B T}\right), \tag{2.1.3}$$

where E_{d} is the desorption energy, k_B is the Boltzmann constant and ν_0 the vibrational frequency of the molecule, typically taken to be in the order of 10^{13}s^{-1}, and is given by

$$\nu_0 = \sqrt{\frac{2n_s E_{\text{d}}}{\pi^2 m_i}}, \tag{2.1.4}$$

where n_s is the surface density of adsorbing sites (Yamamoto, 2017).

2.1.1 Diffusion on surfaces

When an atom overcomes the diffusion energy barrier (E_{diff}), it can migrate to neighboring sites on the surface. This activation energy for diffusion is lower than the adsorption energy (E_{ad}), and both are related as

$$E_{\text{diff}} = \alpha E_{\text{ad}}, \qquad 0 < \alpha \leq 1,$$

where α usually ranges from 0.3 to 1.0 according to experiments (Hama & Watanabe, 2013; Medveď & Černý, 2011).

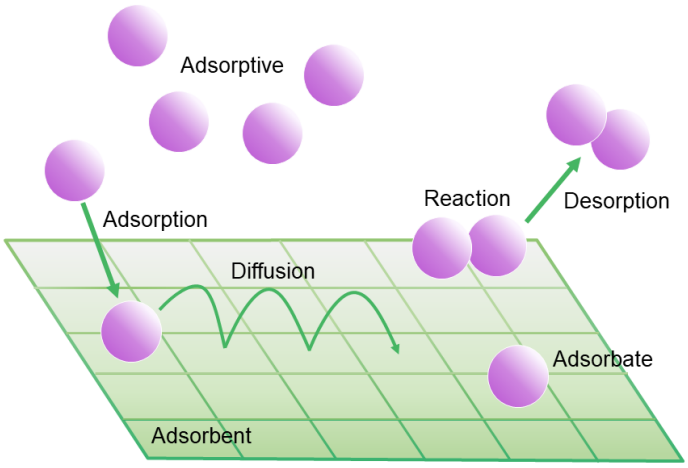

Figure 2.1.2: Illustration showing the interaction between atoms and a surface.

Early models of surface transport suggested that the diffusion flux could be represented with Fick's first law (Gilliland et al., 1974; Naumovets & Vedula, 1985)

$$J = -D\frac{\partial \varphi}{\partial x}, \tag{2.1.5}$$

where D is the diffusivity and φ the surface concentration of particles. The diffusivity can be expressed as an Arrhenius equation (Antczak & Ehrlich, 2007)

$$D = D_0 \exp\left(-\frac{E_{\text{diff}}}{k_B T}\right), \tag{2.1.6}$$

where D_0 is usually a constant given by

$$D_0 = \nu_0 \, \lambda^2 \exp\left(\frac{S_{\text{diff}}}{k_B}\right), \tag{2.1.7}$$

here, λ^2 is the mean-square jump distance and S_{diff} is the entropy of diffusion (Naumovets & Vedula, 1985). The mechanisms mentioned above are sketched in figure 2.1.2.

Quantum tunneling has been proposed as the transport mechanism in the case of light species, such as H or D, at low temperatures (Hama & Watanabe, 2013). For a rectangular barrier of height E_m and width a, the tunneling time is given by (Tielens, 2013)

$$\tau_q = \nu_0^{-1} \exp\left(\frac{2a}{\hbar}(2m_i E_m)^{1/2}\right). \tag{2.1.8}$$

2.2 Physisorption and chemisorption

Adsorption can occur in two different ways: through physisorption or chemisorption. Generally speaking, physisorption is a process in which the electronic structure of the molecule or atom is hardly perturbed, and the corresponding mechanism in molecular physics for this is Van der Waals bonding, therefore the attraction is due to correlated charge fluctuations in the bonding species (Lüth, 2015). This type of adsorption usually occurs when a gas is below its critical temperature (Wiese, 1991) and the energy involved in this process is usually not much larger than the energy of condensation of the adsorbent in the gas phase. This is an exothermic process, therefore, the free energy and enthalpy of the system decrease (Dąbrowski, 2001; Rouquerol et al., 2014). Most neutral species in dense clouds can barrierless physisorb onto ice mantles (Hama & Watanabe, 2013).

In contrast, chemisorption takes place when a chemical bond is formed between the adsorbate and the surface (Lennard-Jones, 1932) and can occur only on the first layer of adsorbed species (Dąbrowski, 2001). An atom can chemisorb to a site in particular on the surface but some diffusion or mobility can also happen. The energy of chemisorption is generally larger than that of physisorption, being the same order of magnitude of the energy change in a comparable chemical reaction (Rouquerol et al., 2014). This process can be exothermic or endothermic. In this type of adsorption there is an activation energy involved, given by $E_a = E_{\text{des}} - E_b$. Figure 2.2.1 shows a schematic of the potential energies for physisorption and chemisorption.

2.3 Surface-reaction mechanisms

After a species is adsorbed, it can react with another atom or molecule through different mechanisms. One of them is the Eley-Rideal (ER) mechanism, where an atom from the gas-phase reacts directly with another atom already chemisorbed on a surface. Some prefer to call this the Langmuir-Rideal mechanism, since it was Langmuir who first proposed it, and refer to Eley-Rideal as the mechanism when there is a reaction between a chemisorbed and a physisorbed species (Kiani & Wachs, 2024; Prins, 2018).

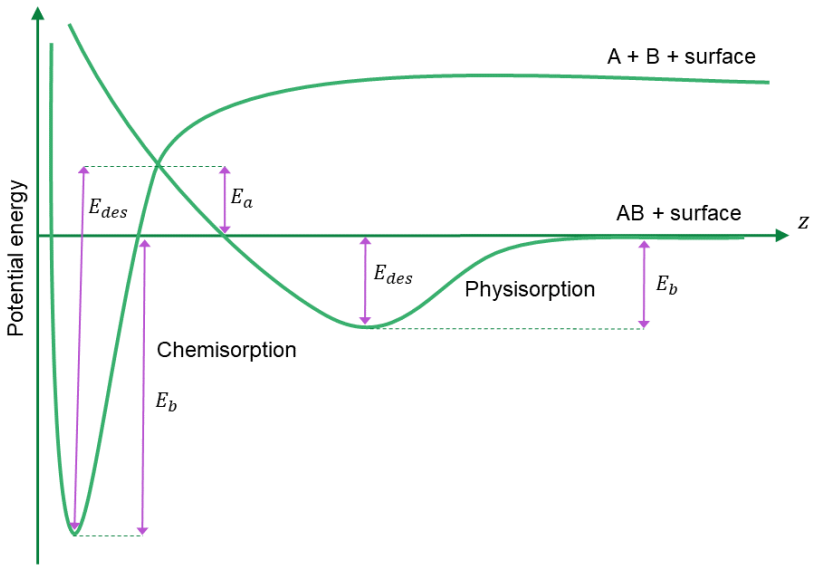

Figure 2.2.1: Lennard-Jones potential of physisorption and chemisorption for a diatomic molecule with distance z from the surface. Dissociative adsorption is considered for chemisorption. Reproduced from Batzill and Diebold, 2005; Potapov and McCoustra, 2021.

The ER mechanism follows the rate law

$$\mathrm{A} + \mathrm{B} \rightarrow \mathrm{P} \qquad r_{\mathrm{ER}} = k_{\mathrm{ER}} p_{\mathrm{B}} \theta_{\mathrm{A}}, \tag{2.3.1}$$

where p_{B} is the partial pressure of the non-adsorbed species B, θ_{A} the surface coverage occupied by the adsorbed species A and k_{ER} is a rate constant. If one knows the isotherm of the adsorbed atom, then the rate law can be written in terms of the partial pressures of both species.

In general, the Eley-Rideal mechanism is considered less relevant in catalysis due to its lower probability of occurring. Despite this, it has been used to explain reactions like the formation of H_2 on dust grains at temperatures greater than 25 K (Le Bourlot et al., 2012). Also, the reaction between H(g) and D(ads) to form HD is thought to be by this mechanism (Atkins et al., 2023).

On the other hand, there is the Langmuir-Hinshelwood (LH) mechanism, where two atoms adsorbed on the surface encounter each other after diffusion and react (figure 2.3.1). The probability of reaction between both species will be proportional

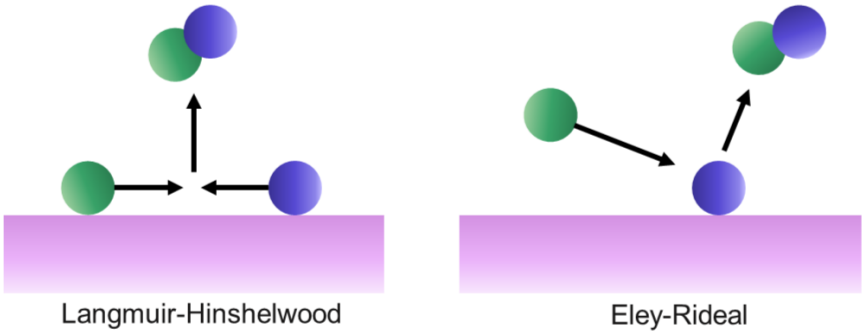

Figure 2.3.1: Two surface mechanisms, Eley-Rideal and Langmuir-Hinshelwood.

to the product between the fractions of occupied sites (Hill, 1977)

$$\mathrm{A} + \mathrm{B} \rightarrow \mathrm{P} \qquad r_{\mathrm{LH}} = k_{\mathrm{LH}} \theta_{\mathrm{A}} \theta_{\mathrm{B}}, \tag{2.3.2}$$

where θ_{A} and θ_{B} are the surface coverage of species A and B, respectively. Figure 2.3.1 shows both of the mechanisms mentioned.

Experiments done through temperature programmed desorption on silicate and amorphous carbon substrates, show that the process of molecular formation on their surface occurs commonly via a diffusive or Langmuir-Hinshelwood mechanism, hence, it is a more relevant process (Baxter & Hu, 2002).

2.4 Temperature programmed desorption

The temperature programmed desorption method (TPD), also known as temperature desorption spectroscopy, consists on thermally activating the energies of desorption (Ibach, 2006). If the temperature is increased linearly, as

$$T(t) = T_0 + \beta t, \tag{2.4.1}$$

where T_0 is the initial temperature, t is time and β is the heating rate (Redhead, 1962) given by $\beta = dT/dt$; the desorption rate is modeled by the Polanyi-Wigner equation

$$-\frac{d\theta}{dt} = \theta^n \nu_0 \exp\left(-E_{\mathrm{d}}/k_B T\right), \tag{2.4.2}$$

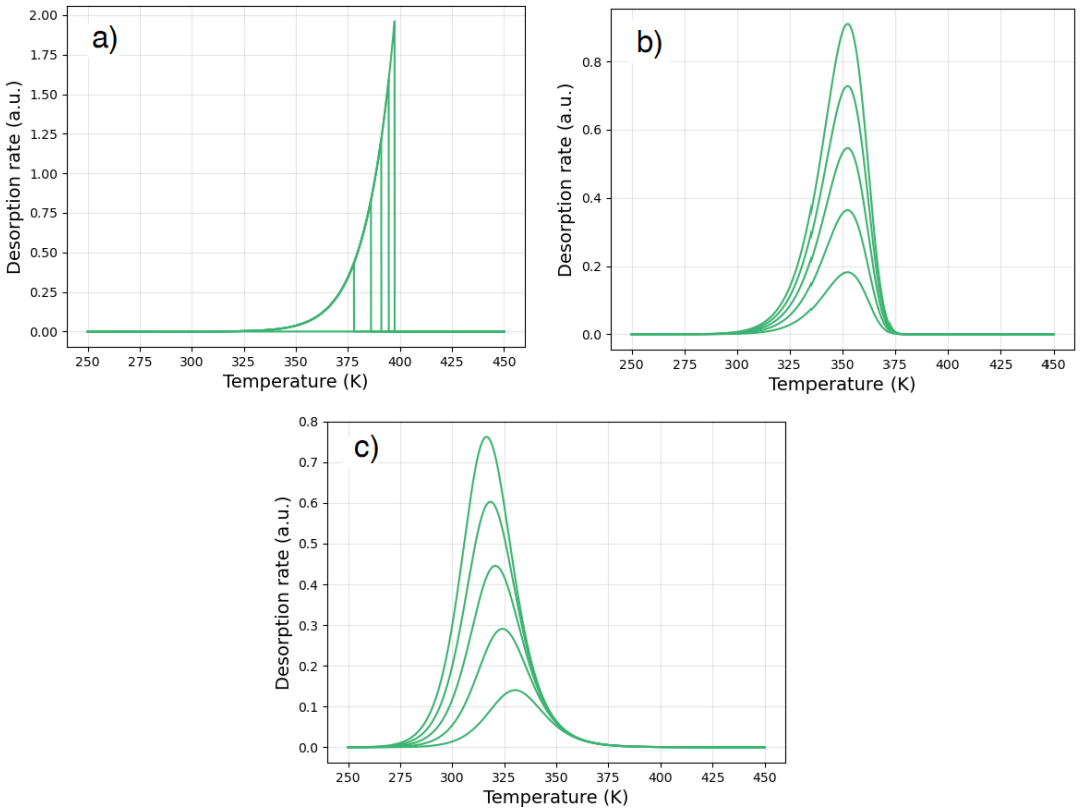

Figure 2.4.1: TPD spectra for a) zero, b) first and c) second desorption order. The simulation was done considering an activation energy of 1 eV, a heating rate of 0.5 K/s and $\nu_0 = 1 \times 10^{13}$ s^{-1}.

which is analogous to equation 2.1.3. Here n is the order of the reaction (Schmid et al., 2023). For $n = 0$, the type of coverage is multilayer; if $n = 1$, the regime is submonolayer and $n = 2$ represents the case of desorption requiring recombination (Ibach, 2006). Figure 2.4.1 shows TPD spectra for each type of order. In these type of experiments, typical heating rates range between 1 K/min and 20 K/min (Ifergane et al., 2018).

2.5 Langmuir's theory of adsorption

In his 1918 paper, Langmuir classified six different models of adsorption according to the characteristics of the binding site and the interactions between adsorbate-surface and occupancy of sites (Langmuir, 1918). His most known model corresponds to the one of single site adsorption. In this model, four main assumptions are made (Ruthven, 1984)

1. The surface has a defined number of sites in which only one molecule can be adsorbed
2. The sites have the same binding energy
3. There is no interaction between neighboring sites
4. The surface is saturated at $\theta = 1$

The adsorption and desorption rates will be

$$k_{\text{ads}} = k_a P(1-\theta) \qquad \text{and} \qquad k_{\text{des}} = k_d \theta, \tag{2.5.1}$$

where P is the partial pressure, this is, the pressure exerted by a specific gas mixture; and k_a and k_d are rate constants for the given system (Atkins et al., 2023; Rouquerol et al., 2014; Ruthven, 1984).

Considering that the system is in equilibrium, adsorption and desorption rates will be equal

$$\begin{aligned} k_a P(1-\theta) &= k_d \theta, \\ \theta &= \frac{k_a P}{k_a P + k_d}. \end{aligned}$$

Taking $K = \dfrac{k_a}{k_d}$, we have the Langmuir isotherm equation

$$\theta = \frac{KP}{KP+1}, \tag{2.5.2}$$

which has an hyperbolic shape, and this can be seen in figure 2.5.1.

The five other classifications proposed by Langmuir were an extension of the single site model. The multiple-site model, assumed that each site had a different binding energy, therefore some would be more favorable for adsorption than others. This could be extended to the generalized Langmuir adsorption model, where the different affinities of the surface towards the adsorbate can be seen as a continuum. The next adsorption classification is the cooperative one, where each binding site is identical but now they can accept multiple molecules. Then, we have dissociative adsorption, which considers the dissociation of a molecule after being adsorbed on a site, to then be able to freely diffuse on the surface; and

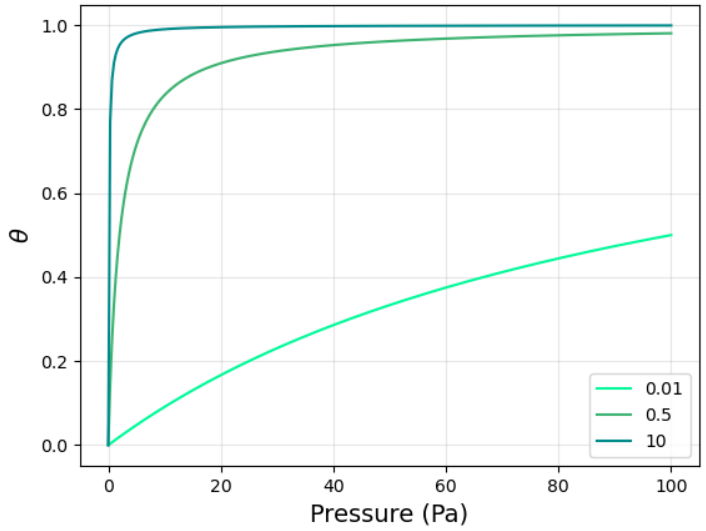

Figure 2.5.1: Langmuir isotherm of single site adsorption for different values of K.

also the reverse process of two atoms forming a molecule and desorbing. Finally, Langmuir described multilayer adsorption, where molecules can adsorb on top of an already adsorbed species, which means that a site could hold a column of infinite adsorbates (Langmuir, 1918; Swenson & Stadie, 2019). The most utilized model for this last case is the Brunauer-Emmett-Teller (BET) theory, which will be discussed next.

2.6 BET theory

As was mentioned before, the BET theory considers a monolayer of adsorbates bound to the surface, allowing the formation of multilayers on top of them. As in the case of single site Langmuir adsorption, there is no interaction between particles on the same layer. The species in the multilayers will be bounded by an energy equivalent to the liquefaction energy of the adsorptive. Then, the BET isotherm equation is

$$\frac{V_T}{V_M} = \frac{C(p/p_0)}{(1-p/p_0)(1-p/p_0+C(p/p_0))}, \tag{2.6.1}$$

where V_T is the total volume adsorbed, V_M is the volume of one monolayer, p is the equilibrium pressure, p_0 the saturation vapour pressure, and the ratio between both of them, p/p_0, is the relative pressure (Brunauer et al., 1938). The constant

C is associated with the binding energy of the first layer E_1 and the energy of the multilayers E_L (Rouquerol et al., 2014), and can be approximated as

$$C \approx \exp\left(\frac{E_1 - E_L}{RT}\right). \tag{2.6.2}$$

If the value of C is high (> 350), then the adsorption energy of the first layer is high and the point B will be sharp in a Type II isotherm. In contrast, when C is low (< 20), then E_1 will also be low and point B is not well defined (Rouquerol et al., 2014).

Equation 2.6.1 can be reordered as

$$\frac{p}{V_T(p - p_0)} = \frac{1}{V_M C} + \frac{C - 1}{V_M C}\frac{p}{p_0}, \tag{2.6.3}$$

which is a more convenient way because the plot of $\frac{p}{V_T(p-p_0)}$ versus $\frac{p}{p_0}$ should give a straight line of slope $\frac{C-1}{V_M C}$ and intercept $\frac{1}{V_M C}$ (Brunauer et al., 1938). For experimental data, this linear plot is observed typically in the range of relative pressures from 0.05 to 0.35.

With this model, one can extract the monolayer capacity of the surface and therefore estimate its specific surface area (Ruthven, 1984). This can be done using the following expression

$$a(\text{BET}) = \boldsymbol{n}_m L \sigma, \tag{2.6.4}$$

where a(BET) is the BET area, $\boldsymbol{n}_m$ is the monolayer capacity, L is the Avogadro number and σ is the area occupied by an adsorbent in the monolayer.

2.7 Types of adsorption isotherms

The ratio between amount of adsorbed gas, n_a, and the mass of solid of the surface m_s will be dependent on the equilibrium pressure, p and the temperature of the system (Rouquerol et al., 2014). For a constant temperature, we can write

$$\frac{n_a}{m_s} = f(p)_T. \tag{2.7.1}$$

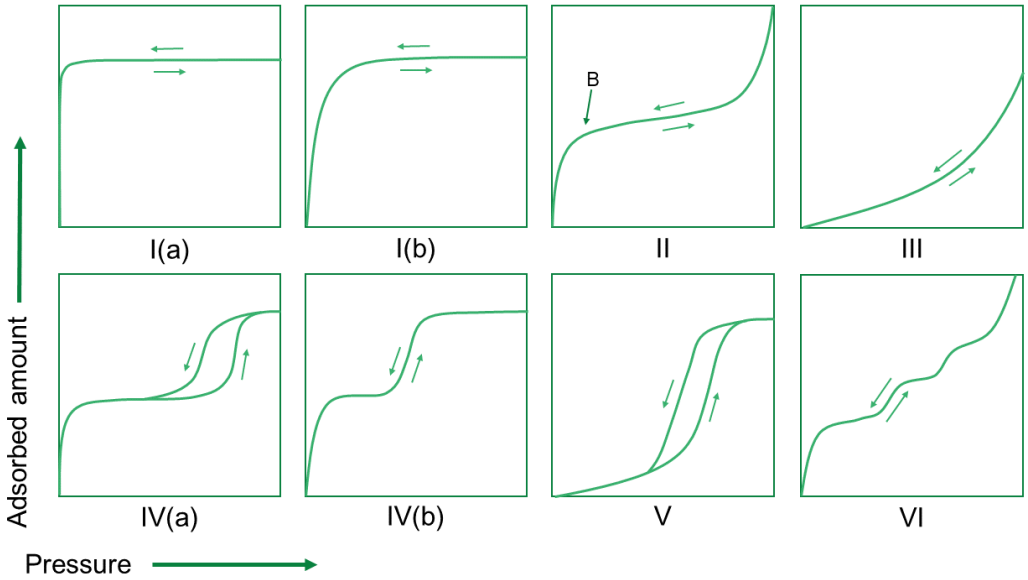

Figure 2.7.1: Types of adsorption isotherms according to IUPAC 2015.

This relation is known as the adsorption isotherm and to measure it, there has to be thermodynamic equilibrium. When the gas is below its critical temperature, we have

$$\frac{n_a}{m_s} = f(p/p_0)_T. \tag{2.7.2}$$

Before determining adsorption isotherms, physisorbed species must be removed from the surface, which can be achieved by outgassing (Thommes et al., 2015).

Isotherm graphs obtained experimentally can be classified in one of six different types of isotherms according to IUPAC 2015 (Thommes et al., 2015), classification that was updated from IUPAC 1985 (Sing, 1985) that included five isotherm types, which itself was inspired by a previous one made by Brunauer, Deming, Deming and Teller in 1940 (Brunauer et al., 1940). Although the addition and modification of isotherm shapes has been proposed by different researchers (Bernet et al., 2026; Donohue & Aranovich, 1999), here we will only consider the ones that appear in IUPAC 2015, shown in figure 2.7.1.

A Type I isotherm graph appears for microporous solids (pores smaller than 2 nm) and it is characterized for having an overall concave shape. At low pressure, a rapid increase of the adsorbed amount can be seen, which is explained by micropore filling. For surfaces with narrow micropores (< 1 nm) one obtains a Type I(a) isotherm, meanwhile a Type I(b) isotherm is characteristic of materials

with a broad arrange of micropore sizes.

Type II isotherms appear for physisorption on macroporous (pores larger than 50 nm) or non-porous surfaces. The concave curve at lower pressures indicates the formation of the firsts layers. For higher pressures, unrestricted formation of multilayers is observed. The point B typically denotes the completion of the first monolayer.

Type III isotherms are also visible in macropores and non-porous material, but in constrast to Type II, here there is no formation of a monolayer. This type of isotherm represents a weaker adsorptive-adsorbent interaction and the adsorbed amount can diverge or not at the saturation pressure.

Mesoporous surfaces (pores between 2 and 50 nm) are the ones that usually give a Type IV isotherm. The curve at low pressures is similar to Type II, which signifies the formation of a monolayer and then multilayers. Most Type IV isotherms are not reversible, and that leads to the formation of an hysteresis loop for $p < p_0$. In this regime of pressure, pore condensation occurs, where the adsorbate trapped in the pores transitions to a liquid phase. For mesopores bigger than a certain width (depending on the adsorbate), an hysteresis cycle is observed, as seen in the Type IV(a) graph. On the other hand, Type IV(b) isotherms are obtained for smaller mesopores and do not exhibit this hyteresis loop, therefore they are reversible. Here, the adsorbate does not undergo a phase transition. In both cases, at high pressures, there is saturation of the adsorbed amount due to the filling of pores.

At low pressures, the curve of a Type V isotherm is similar to that of Type III, since there is no monolayer formation, due to weak gas-surface interactions, and then there is a gradual filling of the pores. This isotherm is observed in mesoporous and microporous adsorbents.

Type VI isotherms exhibit steps that are explained as the formation of multilayers on the surface of non-porous materials. The height of the steps represents the capacity of the layer.

2.8 Henry's Law

At low concentrations, when there are no interactions between neighboring species adsorbed on the surface, there is a linear relation between the fluid and the

adsorbed phase, which is called Henry's law (Ruthven, 1984), expressed as

$$\boldsymbol{n} = k_H p, \tag{2.8.1}$$

where $\boldsymbol{n}$ is the specific surface excess amount, and k_H is the adsorption equilibrium constant also called the Henry constant. This constant can be obtained theoretically, for example, for an inert gas adsorbing on a smooth and energetically uniform surface, it will be

$$k_H = \frac{1}{k_B T} \int_v \exp\left(\frac{-\phi(z)}{k_B T}\right) dz, \tag{2.8.2}$$

where $\phi(z)$ is the potential energy of adsorption as a function of z, the distance between the adsorbate and adsorbant (Rouquerol et al., 2014; Ruthven, 1984).

2.9 Isosteric enthalpy of adsorption

The types of adsorption isotherms seen previously are useful to determine the amount adsorbed on a surface. Now, if we want to characterize the energy involved in the interaction between the adsorbent and the adsorbate, we have to resort to the enthalpy of adsorption. This can be done through the isosteric method, which means measuring multiple adsorption isotherms for different temperatures (Rouquerol et al., 2014). The description presented here follows the one from Rouquerol (2014).

First, we have to take into consideration a few differential quantities of adsorption. One of them is the differential energy of adsorption, which corresponds to the difference between differential surface excess internal energy and the molar internal energy of the ideal gaseous adsorptive

$$\Delta \dot{u}_{T,\Gamma} = \dot{u}^{\sigma}_{T,\Gamma} - u^{g}_{T}, \tag{2.9.1}$$

where Γ is the surface excess concentration.

From this, it can be defined the differential enthalpy of adsorption

$$\Delta \dot{h}_{T,\Gamma} = \Delta \dot{u}_{T,\Gamma} - RT, \tag{2.9.2}$$

and the differential entropy of adsorption would be

$$\Delta \dot{s}_{T,\Gamma} = \frac{\Delta \dot{h}_{T,\Gamma}}{T}. \tag{2.9.3}$$

If equation 2.9.2 is differentiated with respect to T, leaving Γ constant, it yields

$$\left(\frac{\partial \ln [p]}{\partial T}\right)_{\Gamma} = -\frac{\Delta \dot{h}_{T,\Gamma}}{RT^2}, \tag{2.9.4}$$

which is analogous to the Clausius-Clapeyron equation and can be rewritten as

$$\Delta \dot{h}_{T,\Gamma} = R\left(\frac{\partial \ln [p]}{\partial (1/T)}\right). \tag{2.9.5}$$

Now, we integrate this equation over p and T

$$\int_{T_1}^{T_2} \Delta \dot{h}_{T,\Gamma}\, d\left(\frac{1}{T}\right) = R \int_{p_1}^{p_2} d\left(\ln p\right). \tag{2.9.6}$$

Since we are considering only small variations in temperature, one can assume that $\Delta \dot{h}_{T,\Gamma}$ does not vary (Rouquerol et al., 2014). Then,

$$\Delta \dot{h}_{T,\Gamma}\left(\frac{1}{T_2} - \frac{1}{T_1}\right) = R(\ln p_2 - \ln p_1), \tag{2.9.7}$$

$$\Delta \dot{h}_{T,\Gamma} = -\frac{RT_1T_2}{T_2 - T_1} \ln \frac{p_2}{p_1}. \tag{2.9.8}$$

To obtain $\Delta \dot{h}_{T,\Gamma}$, we have to plot $\ln [p]$ for a certain Γ, versus $1/T$, and this is done for a series of isotherms.

Now, for low gas concentrations, it can be noted that the temperature dependence of the Henry constant follows the Van 't Hoff equation

$$\frac{d \ln k_H}{dT} = \frac{\Delta \dot{h}_0}{RT^2}, \tag{2.9.9}$$

where $\Delta \dot{h}_0$ is the differential enthalpy of adsorption for a surface coverage approaching zero (Rouquerol et al., 2014). The plots of $\ln k_H$ versus $1/T$ tend to be practically linear for wide ranges of temperatures (Ruthven, 1984). An example of this is shown in figure 2.9.1.

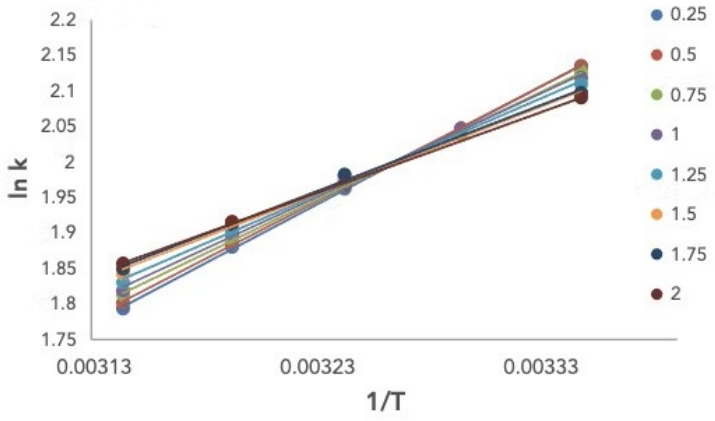

Figure 2.9.1: Van 't Hoff plot of butylbenzene on a C18 column using high performance liquid chromatography for different flow rates in mL/min. From Sepsey, 2022.

The methods mentioned before are already standardized and widely used on isotherm experiments to study surfaces that are relevant in different areas, but they are usually done on wafers or solids with diameters in the range of milimeters. Also, these experiments work in rough vacuum and in a multilayer regime (Magdy et al., 2024; Roles & Guiochon, 1992). As was stated in the introduction, our objective is to transfer this to surfaces of solids in the nanometer range and study sub monolayer coverages, to account for the orders of magnitude of dust in molecular clouds. In this context, a quadropole ion trap that works as a mass spectrometer was used to trap a dust grain analogue, letting us measure mass with femtometers precision. Consequently, these isotherm models are expected to be applied in this setting.

Chapter 3

Quadrupole ion traps and mass spectrometry

The ideal quadrupole ion trap (QIT), also known as Paul traps, have been utilized for a variety of applications, including selective and non-destructive detection of the mass of trapped ions and confinement of ions for long periods of time. The theory presented here is based on the behavior of one ion in an infinite ideal quadrupole field (March & Todd, 2005; Schlemmer et al., 2001).

Particles can be confined in a volume due to an attractive force that increases linearly with distance,

$$\vec{F} = -k\vec{r} = -\nabla\phi(x, y, z)$$

where k is a constant.

Inside the device, the potential in a given point will depend on the square of the distance from the origin. In cartesian coordinates, we have

$$\phi_{x,y,z} = A(\eta x^2 + \sigma y^2 + \gamma z^2) + C, \tag{3.0.1}$$

where A is independent from the coordinates that accounts for the electric potential applied to the electrodes, C is a fixed potential; and η, γ and σ are weighting factors.

In a region free of charges, the Laplace equation is satisfied

$$\nabla^2\phi_{x,y,z} = 0. \tag{3.0.2}$$

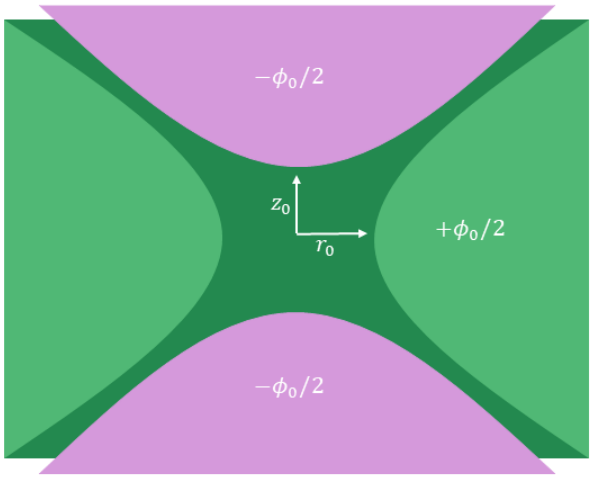

Figure 3.0.1: Geometry of the QIT, reproduced from Esser et al., 2019.

By replacing equation (3.0.1) in equation (3.0.2) we obtain

$$\eta + \sigma + \gamma = 0.$$

There are infinite combinations that fulfill this, but the values usually used for the QIT are

$$\eta = \sigma = 1 \qquad \text{and} \qquad \gamma = -2.$$

An ideal QIT is composed by 3 electrodes, two of them are end-cap electrodes with hyperboloid geometry, and the third one is the ring electrode, that is placed in the middle and has an internal hyberboloid surface (figure 3.0.1). So, the surface of ring electrode is given by

$$\frac{r^2}{r_0^2} - \frac{z^2}{a^2} = 1, \tag{3.0.3}$$

where $m = \pm a/r_0$, and for the end-cap electrodes we have

$$\frac{r^2}{b^2} - \frac{z^2}{z_0^2} = -1, \tag{3.0.4}$$

where $m' = \pm z_0/b$.

To stablish a quadrupole field, the electrodes must share asymptotes, $m = m'$. From this we find that $\phi_{r,z}$ becomes constant when $b^2 - 2z_0^2 = 0$, then $b^2 = 2z_0^2$, which implies that $a^2 = r_0^2/2$. With this, $m = \pm 1/\sqrt{2}$.

Then, equations 3.0.3 and 3.0.4 become

$$\frac{r^2}{r_0^2} - \frac{2z^2}{r_0^2} = 1 \qquad \text{and} \qquad \frac{r^2}{2z_0^2} - \frac{z^2}{z_0^2} = -1,$$

respectively.

We have

$$\phi_{r,z} = A(r^2 - 2z^2) + C, \tag{3.0.5}$$

and we can also define

$$\phi_0 = \phi_{\text{ring}} - \phi_{\text{end-caps}}.$$

When $z = 0$, then $r = \pm r_0$, and when $r = 0$, $z = \pm z_0$. Replacing in 3.0.5

$$\phi_{\text{ring}} = A(r_0^2) + C, \qquad \phi_{\text{endcaps}} = A(-2z_0^2) + C,$$

therefore

$$\phi_0 = A(r_0^2 + 2z_0^2).$$

From here, we can find A and substitute in 3.0.5.

$$\phi_{r,z} = \frac{\phi_0(r^2 - 2z^2)}{r_0^2 + 2z_0^2} + C.$$

Constant C is evaluated considering the potentials connected to the electrodes. The end-cap electrodes can be held at ground, and a unipolar RF or any DC voltage can be applied to the ring electrode. So,

$$\phi_{0,z_0} = \phi_{\text{endcaps}} = \frac{\phi_0(0 - 2z_0^2)}{r_0^2 + 2z_0^2} + C = 0, \tag{3.0.6}$$

that yields

$$C = \frac{2\phi_0 z_0^2}{r_0^2 + 2z_0^2}.$$

Then we have the following potential

$$\phi_{r,z} = \frac{\phi_0(r^2 - 2z^2)}{r_0^2 + 2z_0^2} + \frac{2\phi_0 z_0^2}{r_0^2 + 2z_0^2}. \tag{3.0.7}$$

This way of connecting the electrodes has the effect of halving the maximum value of the m/z of the ions that can be stored. So, considering a real system we can

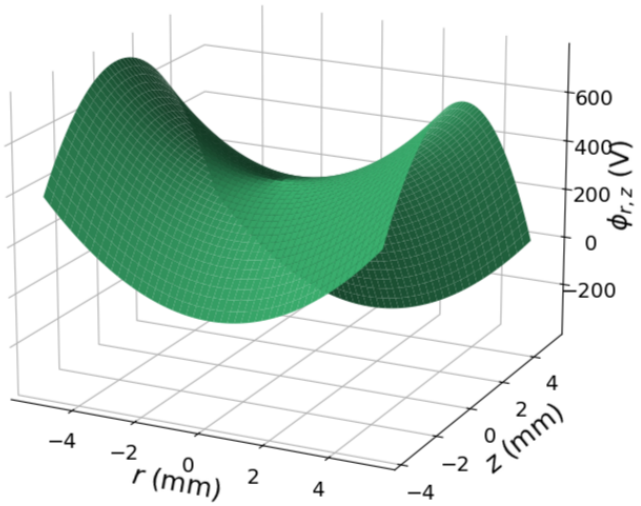

Figure 3.0.2: Shape of the quadrupole potential inside the trap.

define

$$\phi_0 = U + V\cos\Omega t,$$

where V corresponds to the zero to peak amplitude of a RF potential oscillating with angular frequency Ω and U is a DC voltage.

As the coefficients η, σ, γ do not have all the same sign, the force can not be attractive in all 3 dimensions for a static potential, therefore, due to the inhomogeneity of the field, particles experience a changing force field in their motion, causing a net force towards the center of the trap. Replacing in 3.0.7 yields

$$\phi_{r,z} = \frac{(U + V\cos\Omega t)(r^2 - 2z^2)}{r_0^2 + 2z_0^2} + \frac{2(U + V\cos\Omega t)z_0^2}{r_0^2 + 2z_0^2},$$

and this potential has the shape shown in figure 3.0.2.

Considering that

$$F_z = -e\left(\frac{d\phi}{dz}\right)_r = e\frac{4\phi_0 z}{r_0^2 + 2z_0^2} = m\left(\frac{d^2z}{dt^2}\right),$$

we have

$$\frac{d^2z}{dt^2} = \left(\frac{4eU}{m(r_0^2 + 2z_0^2)} + \frac{4eV\cos\Omega t}{m(r_0^2 + 2z_0^2)}\right) z.$$

It can be noted that this similar to the Mathieu equation

$$\frac{d^2u}{d\xi^2} + (a_u - 2q_u\cos 2\xi)u = 0. \tag{3.0.8}$$

Then, we can make the variable change $t = 2\xi/\Omega$, that will yield

$$\frac{d^2z}{d\xi^2} = \left[\frac{16eU}{m(r_0^2 + z_0^2)\Omega^2} + \frac{16eV\cos(2\xi)}{m(r_0^2 + z_0^2)\Omega^2}\right] z.$$

Therefore, we have

$$\frac{16eU}{m(r_0^2 + z_0^2)\Omega^2} + \frac{16eV\cos(2\xi)}{m(r_0^2 + z_0^2)\Omega^2} = -a_z - 2q_z\cos(2\xi),$$

and from this it is deduced that

$$a_z = -\frac{16eU}{m(r_0^2 + 2z_0^2)\Omega^2} \qquad \text{and} \qquad q_z = \frac{8eV}{m(r_0^2 + 2z_0^2)\Omega^2}.$$

If we do the same with the radial component, we find that

$$a_z = -2a_r \qquad \text{and} \qquad q_z = -2q_r.$$

The solutions to the Mathieu equations are either periodic but unstable or periodic but stable. Solutions of the former type, form the limits of the unstable regions in the stability diagram. These limits correspond to integer values of the trapping parameter β_z.

Stable solutions will determine the trajectory of the ions inside the trap. In figure 3.0.3 are shown the stability regions for the r and z components. The superposition of these two regions yields the complete stability diagram, that determines the conditions for an ion to be trapped. The stable trajectory we consider is obtained in the region closer to the origin in the graph.

A tridimensional representation of the motion of an ion in a trap has the general appereance of a Lissajous curve, as seen in figure 3.0.4. The motion of the ion in the radial and axial directions consist of a smooth secular motion and a more

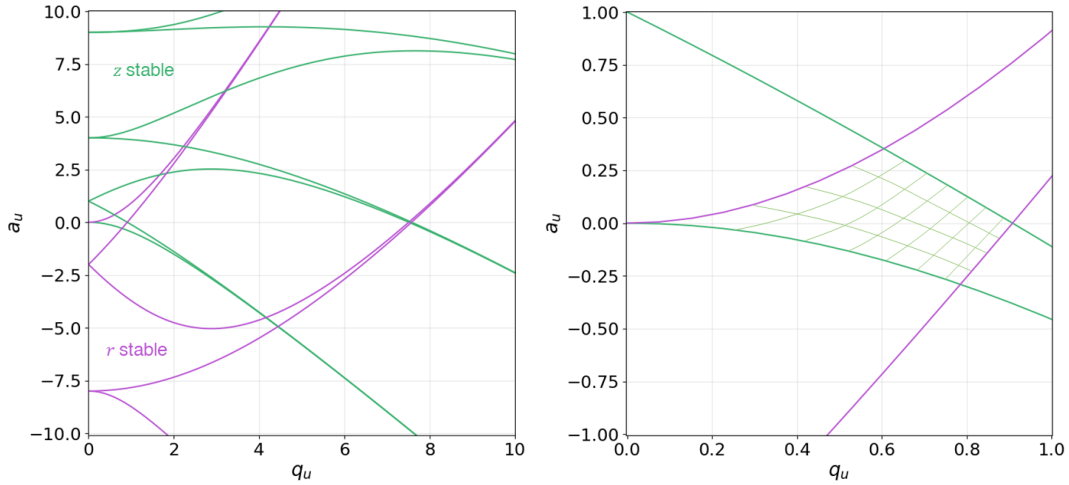

Figure 3.0.3: (Left) Stability diagram for the solutions of the Mathieu equation. The zone denoted by green corresponds to the z-stable region and the zone denoted by pink corresponds to the r-stable region. The overlap of both regions gives us the conditions for stable solutions. The r-stable region is obtained by -2 times the z-stable region. (Right) Close up of the first stable region. In light green are shown the iso-β_u lines.

rapid oscilation, at a trap frequency Ω. The secular frequencies are given by

$$\omega_{u,n} = \begin{cases} -\left(n + \frac{1}{2}\beta_u\right)\Omega, & -\infty < n < 0 \\ \left(n + \frac{1}{2}\beta_u\right)\Omega, & 0 \leq n < \infty \end{cases}$$

where

$$\beta_u \approx \sqrt{a_u + \frac{1}{2}q_u^2}$$

for $q_u < 0.4$. Only the fundamental frequencies will be relevant here, hence, we have $\omega_{z,0} = 2\omega_{r,0} = \frac{1}{2}\beta_z\Omega$.

Now, if we take $U = 0$, then $a_u = 0$, we get

$$\begin{aligned} \omega_{r,0} &= \frac{1}{2}\beta_r\Omega \\ &= \sqrt{2}\,\frac{eV}{m(r_0^2 + 2z_0^2)\Omega}, \end{aligned}$$

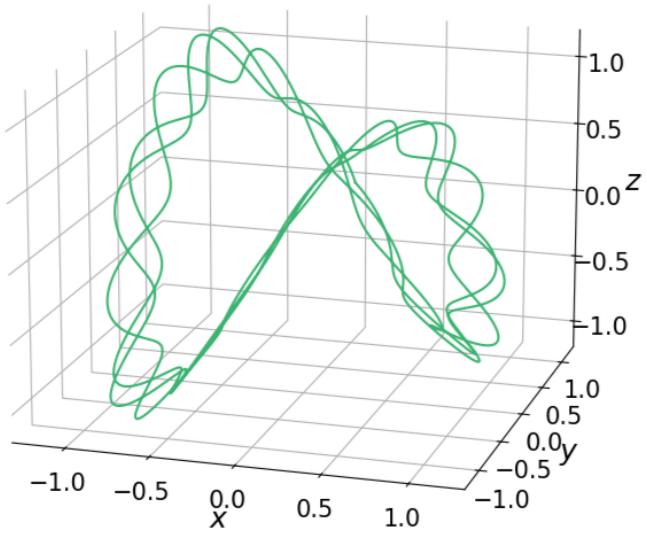

Figure 3.0.4: Motion followed by the particle due to the potential in the trap. The trajectory is composed of a typical Lissajous curve (figure-8 like path) and a micromotion.

and

$$\begin{aligned}\omega_{z,0} &= \frac{1}{2}\beta_z\Omega \\ &= \frac{4eV}{\sqrt{2}m(r_0^2+2z_0^2)\Omega}.\end{aligned}$$

From here, it is possible to find the mass to charge ratio in terms of the fundamental frequencies

$$\frac{m}{e} = \frac{2\sqrt{2}\,V}{\omega_z(r_0^2+2z_0^2)\Omega}. \tag{3.0.9}$$

Chapter 4

The CODE setup

Figure 4.0.1 shows the experimental setup of CODE. The vacuum chamber in the middle has eight ports, out of which seven are used at the moment: one for the vacuum pumps, gas injection, electrical feedtrough, two viewports for optical access, a viewport to check inside the chamber, and a T connector with the electron gun and a pressure gauge. Inside the enclosure at the back, lays the optical setup of the experiment.

4.1 Vacuum and gas inlet system

The vacuum system features a dry scroll pump (IDP-15, Agilent) and a turbomolecular pump (Twistorr 305 FS, Agilent), the latter being controlled through the CODE program. To measure pressure we use an inverted magnetron pirani gauge (FRG-702, Agilent) and a barometer monitor (XGS-600 Gauge Controller, Agilent). The minimum pressure we have been able to reach at room temperature is of 10^{-6} torr.

Figure 4.1.1 shows the gas lines that allow the injection of five different gases in the chamber. At the moment only argon has been injected, being used as the buffer gas in the system. The amount of argon injected is controlled through a leak valve connected to one of the ports of the chamber.

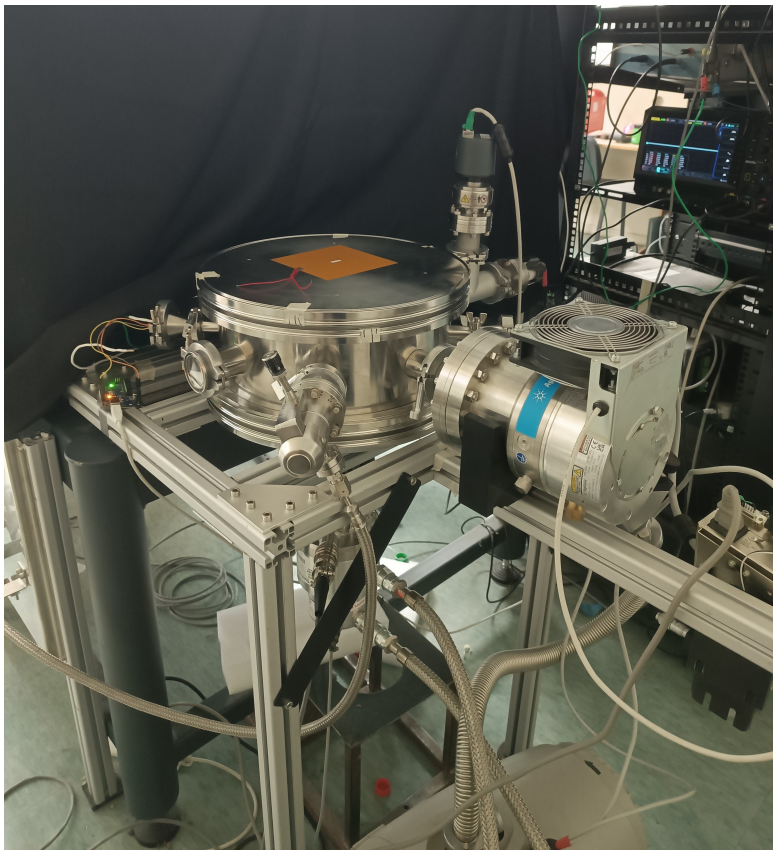

Figure 4.0.1: The CODE experimental setup.

Figure 4.1.1: Gas lines.

4.2 Split ring electrode trap

To be able to detect and have better control over the nanoparticle, the ion trap used in this experiment is a bit different from a normal quadrupole trap. Instead of having two end-cap electrodes and one ring electrode in the middle, we use a trap that has four electrodes in total: two at the top and two at the bottom. This leaves an open space in the middle of the trap, allowing better optical access to the sample.

The design of this split ring electrode trap (SRET) was inspired by a design previously done by Esser et al., 2019, which itself was inspired in designs by Howder et al., 2014 and Gerlich and Decker, 2014; but these used a total of six electrodes (three at the top, three at the bottom) instead of four. The dimensions of the trap are $z_0 = 3.69$ mm and $r_0 = 5.22$ mm, that essentially mantain the relation $r_0^2 = 2z_0^2$ considered for ideal Paul traps, therefore, the equations used to determine the mass to charge ratio remain the same.

Figure 4.2.1 shows the ion trap attached to the coldhead. The elctrodes of the trap were made from copper and the mount was made with PEEK plastic, which has low outgassing, therefore is useful for ultra high vacuum experiments.

The trap is located in the center of the vacuum chamber, such that the electron gun, the laser and the detection system have direct access to the center of the trap, where particles are stored.

The signal applied to the electrodes corresponds to a sinusoidal one, generated by a signal generator connected to a voltage amplifier, that can amplify the voltage by 200 times. With this, the maximum voltage that can be applied to the electrodes is 1600 Vpp. Regarding the frequency of the trap, it can be set up to a maximum of 200 kHz, but is usually set between 600 and 2000 Hz in vacuum conditions.

The optimum voltage and frequency will depend on whether we are at atmospheric pressure or in vacuum, and also on the size of the particle. Usually, low frequency and high voltage is best for atm and to trap particles of high mass; and on the contrary, high frequency and lower voltage is used in high vacuum and for trapping lighter particles.

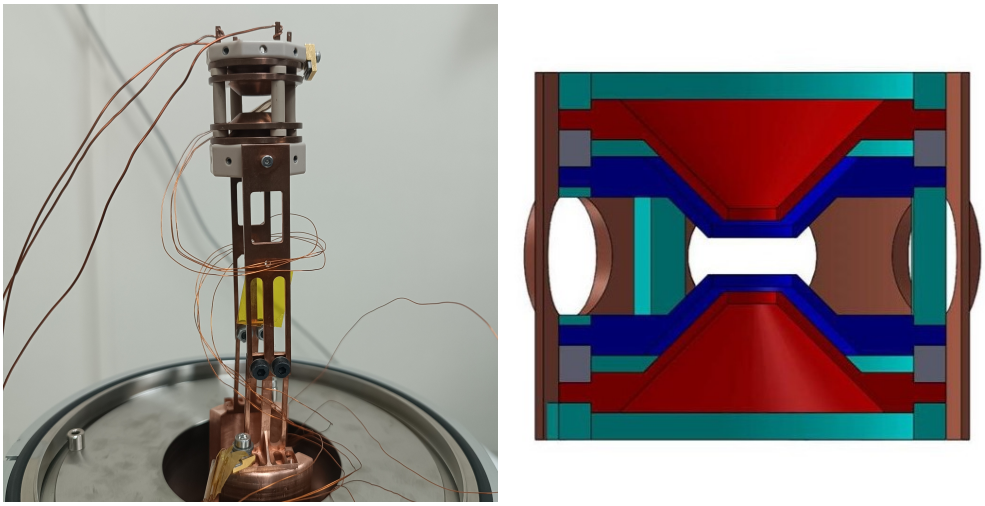

Figure 4.2.1: Split ring ion trap. On the left, an actual picture of the trap connected to the coldhead, and on the right, a cross section of the 3D model of the trap.

4.3 Nanoparticles

Amorphous silica (SiO_2) was chosen as the dust grain analogue, due to the relevance of amorphous silicate species in dense interstellar clouds. The particles used in the experiment were made in a bottom-up way through a sol-gel process, which allows us to control the size and distribution of the particles produced (Rahman & Padavettan, 2012). We used the Stöber method, which produces monodisperse silica particles in sizes that can range from about 0.05 to 2 μm (Stöber et al., 1968). Different mixtures can be used to obtain silica particles, but in our case the reactants included ammonia, water, tetraethyl orthosilicate (TEOS) and ethanol. The particles obtained had a 160 nm diameter, with a fairly uniform distribution. Figure 4.3.1 shows an electron microscope image of the particles.

In the process of synthesizing nanoparticles, silanol groups are formed due to the hydrolysis of the TEOS molecules. These groups have the form Si-O-H, and the polymerization between them create the bridges that form the silica structure (Rahman & Padavettan, 2012). A lot of the hydroxyl groups (-OH) are retained at the end of the structure (T. G. Kim et al., 2017), which make the surface hydrophilic and can contribute to particle agglomeration (Cheng et al., 2020). Research has shown that the -OH layers can be reduced with thermal treatment, with great improvement between temperatures from 100 to 600°C (Li et al., 2024;

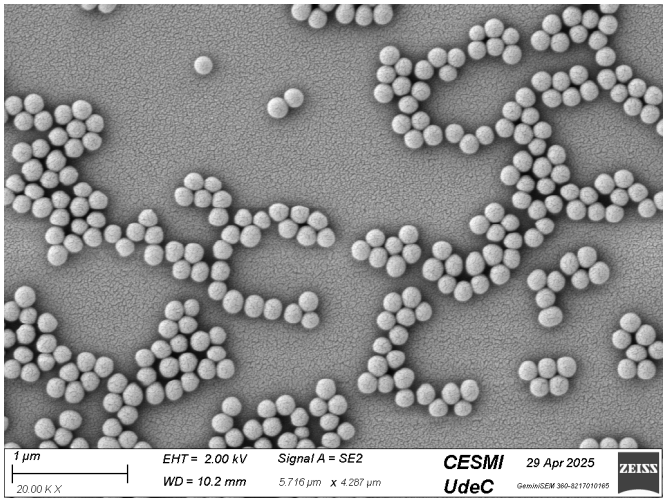

Figure 4.3.1: SiO_2 particles seen in an electron microscope.

Peng et al., 2009). However, after being in contact with ambient humidity, the OH layer around the silica nanoparticles might form again (Paparazzo et al., 1992).

Figure 4.3.2 shows three Fourier-transform infrared (FTIR) spectra for silica particles in different conditions. The peaks around 472 cm^{-1} are due to the rocking of Si-O-Si, the ones at 800 and around 1100 cm^{-1} correspond to its symmetric and asymmetric stretching, respectively. The bands around 948 cm^{-1} are because of the stretching of Si-OH groups, and the ones around 1630 and 3430 cm^{-1} are due to H-OH vibrations (T. G. Kim et al., 2017; Li et al., 2024). In the case of the liquid sample, there are small peaks around 2900 cm^{-1} that can be due to residual alcohol (Almeida & Pantano, 1990).

4.4 Injection system

We have tried three different injection methods in CODE: electrospray ionization (ESI), an arduino actuated brush and a loudspeaker. So far, the brush has been the only method that has allowed us to successfully trap particles. In the following, each method will be reviewed.

4.4.1 ESI

Electrospray ionization is a technique used to convert solution-phase species into ionized gas (Konermann et al., 2013), so particles are charged before being introduced into a mass spectrometer. The solution goes through a metal capillary

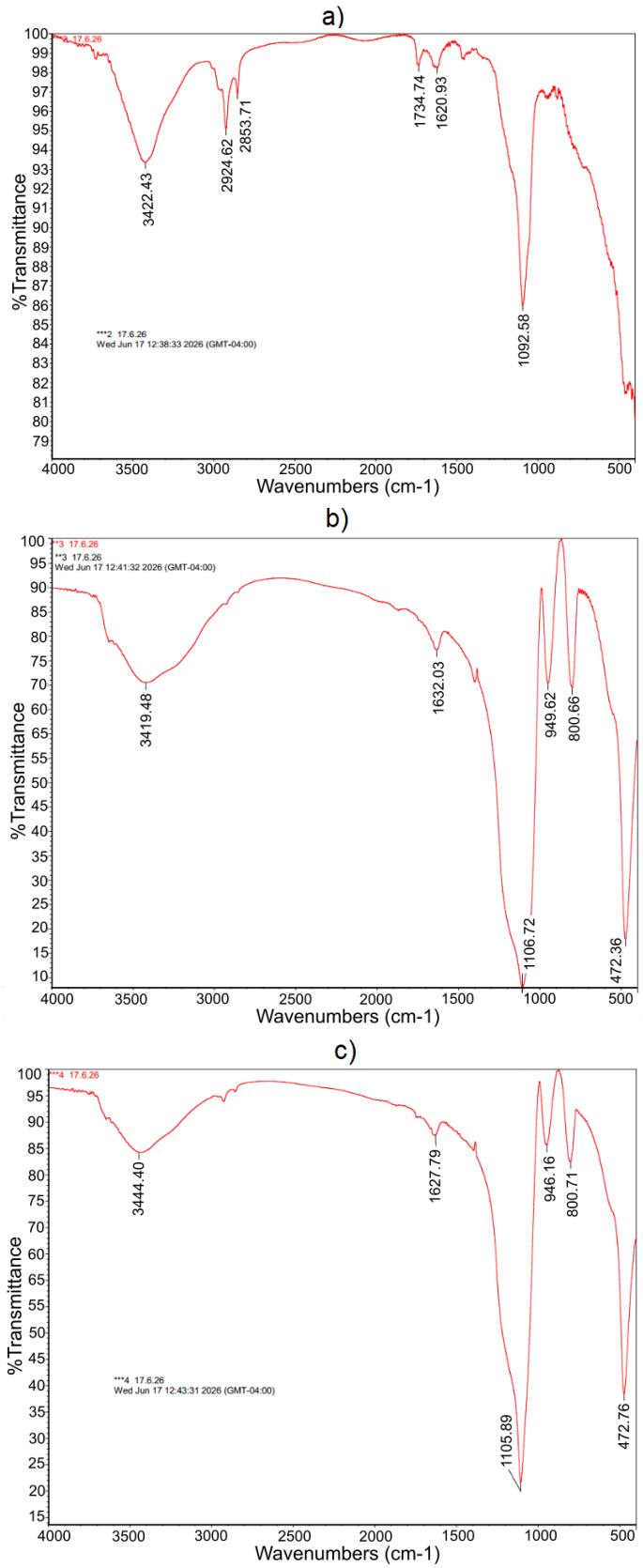

Figure 4.3.2: FTIR spectra of three different silica samples. a) corresponds to a liquid solution, b) is for air dried particles and c) for particles dried at 70°C.

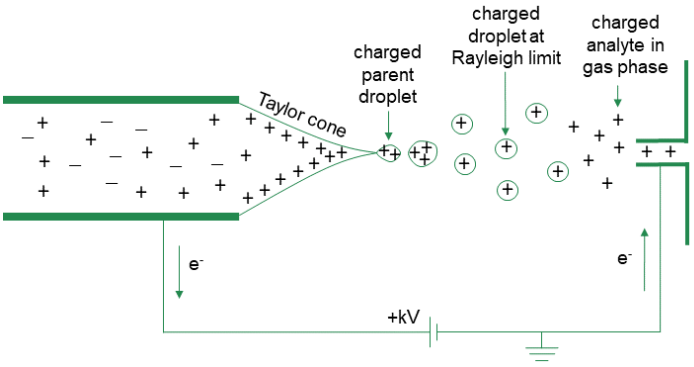

Figure 4.4.1: Illustration of the ESI and the stages the ions go through.

held at an electric potential of a few kV (Liuni & Wilson, 2011). The solution is injected into the emitter with a syringe pump at flow rates that are in the range of nL/min. When the potential is positive, the particles coming out of the emitter create an excess of positive charge that ends up creating a Taylor cone, as shown in figure 4.4.1. At the end tail of the cone, when coulombic repulsion balances surface tension, the Rayleigh limit is reached, where the number of elementary charges is

$$z_R = \frac{8\pi}{e}\sqrt{\varepsilon_0 \gamma R^3}, \tag{4.4.1}$$

where ε_0 is the vacuum permittivity, γ the surface tension and R the radius of the droplet. At this limit, the droplets undergo through jet fission, producing smaller droplets that are highly charged (Konermann et al., 2013; Liuni & Wilson, 2011). With each fission event, droplets lose a percentage of mass and charge, until reaching a radius of few nanometers before entering the counterelectrode leading to the chamber. Figures 4.4.2 and 4.4.3 show the ESI system and the droplets af analytes.

There are two mechanisms through which ionization can occur, Charged Residue Model (CRM) and Ion Evaporation Model (IEM). The IEM is usually considered in the case of smaller analytes, and it predicts that when the droplet shrinks to a radii smaller than 10 nm, there will be direct ion emission without Coulomb fission (Kebarle & Verkerk, 2009). On the other hand, the production of ions of macromolecules or bigger species is probably due to CRM, which assumes that when a droplet containing one macro molecule evaporates, the charge of the droplet is transferred to the molecule (Kebarle & Verkerk, 2009). In this case, the droplet stays close to the Rayleigh limit, between a 75 to 95%.

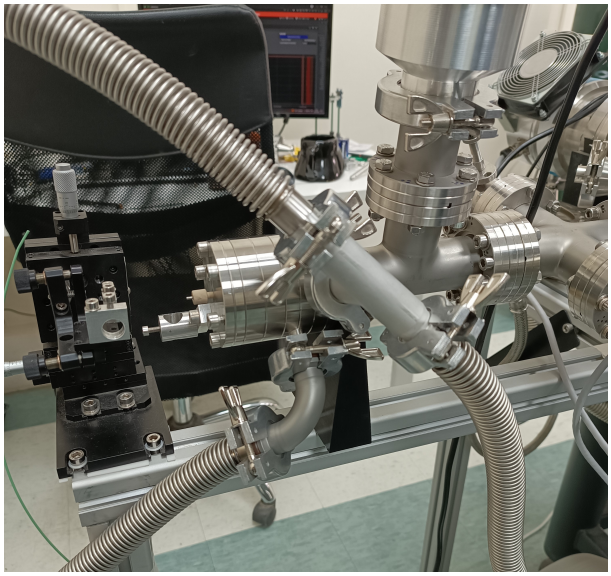

Figure 4.4.2: ESI connected to the rest of the experiment.

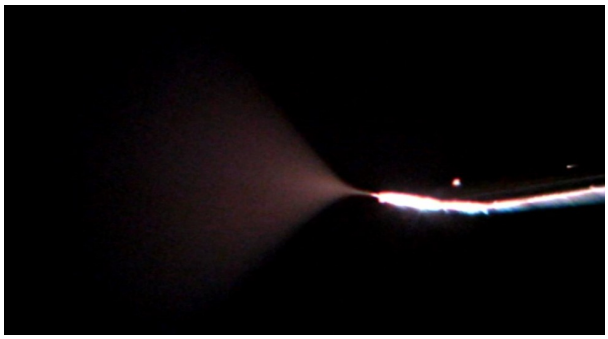

Figure 4.4.3: Charged droplets coming out of the needle. The flow rate was set to 550 nL/min and the voltage to 3710 V. The mixture was 9:1 ml of distilled water to particle concentration.

It must be noted that these two models are not mutually exclusive (Liuni & Wilson, 2011), although for our case we can consider only the charged residue model, because the radius of the nanoparticles is ∼80 nm.

As ESI is a common technique used in mass spectrometry experiments (Esser et al., 2019; Ho et al., 2003), it is our best option for injecting particles into the chamber. However, the particles gain great speed (close to the speed of sound) and the buffer gas is not enough to make them slow down before reaching the ion trap. While more tests regarding ESI need to be done, to continue moving forward with the experiment, we have proposed different injection methods that involve ionizing the particles through triboelectric charging.

4.4.2 Brush

In this method, a brush made with nylon fibers is loaded with dried silica particles that are placed in a glass petri dish. The brush is then positioned above the top electrode of the trap and actuated through an arduino (Arduino UNO). The motion of the brush against the electrode makes the particles fall into the center of the trap.

This method works thanks to triboelectric charging, a topic that still has many open questions regarding what properties of the materials are responsible for this phenomenon and its modeling (Lacks & Shinbrot, 2019). Research has led scientists to make different assumptions, for example, the existence of a triboelectric series, a way of categorizing materials on whether they are more likely to charge positively or negatively depending on the material they are rubbed against (Lacks & Shinbrot, 2019; Pan & Zhang, 2019). This way of classification has been around since the 18th century and is purely empirical. It has been noted though that this model is not always accurate, and that triboelectric charging can also be influenced by other aspects, such as changes in the morphology of the material (Shaw & Jex, 1928). Other findings have established that hydrophilic surfaces tend to charge positively after contact with an hydrophobic material (Lee et al., 2018); and also that in granular material of the same composition, smaller particles tend to get negatively charged meanwhile larger particles get a positive charge (Lacks & Shinbrot, 2019).

Charge transfer will also depend on whether the materials in contact are metals or insulators. In the case of insulator-insulator contact, one model assumes that on the surface there is an available energy level for electrons, called the surface state (Matsusaka et al., 2010). Assuming the insulators have an apparent effective work, the difference between the effective work of insulator 1 (ϕ_1) and insulator 2 (ϕ_2) will drive electrons in one surface state to move to the empty spaces of the other surface state. When the Fermi levels of both materials are equal, the exchange will stop (Anderson, 1994; Matsusaka et al., 2010). The equation that gives us the equilibrium condition for the energy levels can be expressed as

$$\phi_1 + \Delta_1 + eE_f z_m = \phi_2 - \Delta_2, \tag{4.4.2}$$

where Δ_1 and Δ_2 correspond to change in Fermi energy of each insulator, E_f is

the electric field between both materials, z_m is the effective separation distance and e is the charge (Castle & Schein, 1995; Matsusaka et al., 2010).

As it is difficult to describe the triboelectric charging of materials, to analyze our situation we must first take certain factors into account concerning the charge of SiO_2. For example, under aqueous suspension, silica tends to be negatively charged, although this is also influenced by the pH of the solution (An et al., 2014). Nevertheless, when dried, silica will not necessary carry a fixed net charge and the charging will mostly depend on contact, friction and humidity (Gouveia et al., 2008).

Out of all the contact processes that are carried out: silica-petri dish, silica-brush, brush-electrode; one could argue that the one that contributes the most in charging the particles is the one between the brush and the silica, since it is the process with the most interaction between materials. According to the triboelectric series, nylon 66 is placed below silica (Y. J. Kim et al., 2017), thus silica would get positively charged and the brush would be negatively charged when rubbed together. As was stated previously, the triboelectric series approach is not always accurate. Another point of view would be to consider the transfer of OH^- ions from silica to the nylon bristles, leading to the same conclusion as before (Lee et al., 2018).

As reported by articles on experiments involving the trapping of silica (Frimmer et al., 2017; Schlemmer et al., 2004; Schlemmer et al., 2001), the nanoparticles carry up to several tens of positive elementary charges when trapped. This is in agreement with the prior made inference.

Figure 4.4.4 shows an illustration of the brush above the trap and a SEM image of a sample of the particles.

The brush injection method has been useful in CODE since it has allowed us to make our first measurements. Nevertheless, it still presents some drawbacks, as we have to turn off the vacuum every time the brush needs reloading. Also, there is a risk that foreign air dust particles get attached to the bristles whenever we take the brush out of the chamber. This has lead us to implement a new injection mechanism: a loudspeaker that impulses the particles from the bottom of the trap, and therefore does not need to get recharged with particles as often.

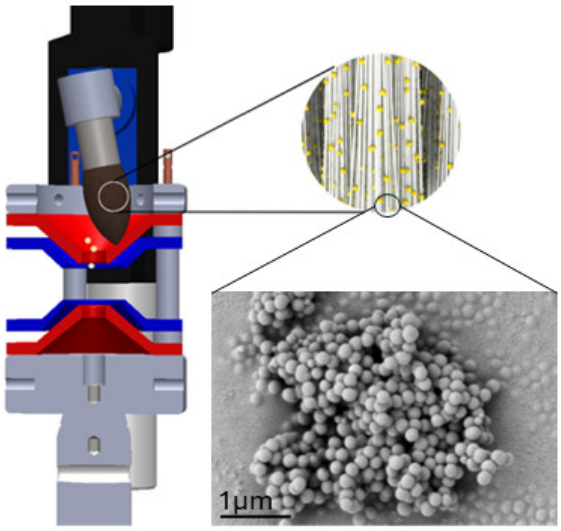

Figure 4.4.4: Illustration of the injection system and electron microscope image of a cluster of particles after falling from the brush. From Martínez Sepúlveda et al., 2026.

4.4.3 Loudspeaker

The last injection method consists in throwing the particles from the bottom with a loudspeaker, considering that the trap is attached to the coldhead that is placed on top of the chamber. This method has been used in different mass spectrometry experiments before, as can be seen in Schlemmer et al., 1999, 2001 and Grimm et al., 2006. In the case of CODE, the system is still undergoing troubleshooting and has not been fully implemented yet.

A couple of different ways of integrating this have been envisioned. For example, placing the particles on a small plate glued to a metal sheet actuated by the vibrations of the loudspeaker, that would act as a catapult to launch the nanoparticles. However, the most recent version of this injection mechanism consists on replacing the diaphragm of the loudspeaker with a rubbery material so particles are placed on top of it, and using neodymium magnets stronger than the original ones of the loudspeaker.

4.5 Optical setup and data acquisition

The optical setup, shown in figure 4.5.1, consists mainly of three elements: a 532 nm laser (LSR532NL Civil laser 500mW) that illuminates the particle, a camera

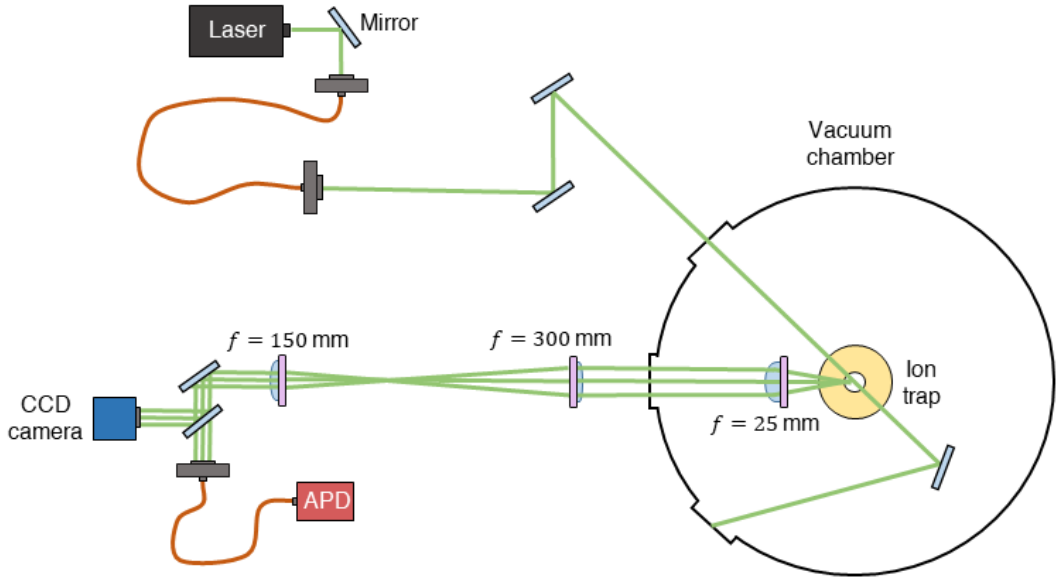

Figure 4.5.1: Sketch of the optical setup of the experiment.

that allows us to see the center of the trap and an avalanche photodiode (APD) that detects the secular frequencies of the particle's motion. The laser first goes through a single mode fiber, coming out with a power of ∼15 mW, and then it goes into the vacuum chamber through a view port, reaching the center of the ion trap and being redirected with a mirror so it does not reflect inside of the chamber. The light scattered by a trapped particle then passes three plane-convex lenses, with focal points of 25 mm, 300 mm and 150 mm, respectively. After this, the light can either be directed to the APD or to the camera, depending on the position of a mirror with a flip mount that is in between. Figure 4.5.1 shows a schematic of the optical setup.

The interaction between the laser and the particle can be modeled with Rayleigh scattering, since the size of the nanoparticle is smaller than the wavelength of the light. Thus, the scattering force exerted on a dielectric spherical particle is given by

$$\boldsymbol{F}_{\text{scat}}(\boldsymbol{r}) = \frac{I(\boldsymbol{r})\alpha n_p}{c}\hat{z}, \tag{4.5.1}$$

where

$$\alpha = \frac{128\pi^5 a^6}{3\lambda^4}\left(\frac{m^2-1}{m^2+2}\right)^2, \tag{4.5.2}$$

and $m = n_p/n_m$. In these equations, $I(\boldsymbol{r})$ is the intensity of the light, c the speed of light, a is the radius of the particle, and n_p and n_m are the index of refraction

Figure 4.5.2: Display of the counts and frequencies detected by the APD seen on the CODE control program, with a resolution of 0.1 Hz.

of the particle and the medium, respectively.

4.5.1 Detection of the nanoparticle

The light scattered by the particle is collected by an APD (COUNT-250N, Laser Components), which is connected to an FPGA that reads the signal. The number of counts detected by the APD and the Fourier transform of the secular frequencies of the trapped nanoparticle can be displayed in the CODE program, as seen in figure 4.5.2. The program has a data logging tab, where one can select the information to be stored and define for how long the program will be storing data. There is also an option to set the number of samples of FFT and how they are going to be averaged. The data is saved in a HDF5 file that can then be read and displayed with a python program. The data stored can have a resolution of 0.1 to 0.01 Hz.

To see the trapped particle we use a charge-coupled device (CCD) camera. Figure 4.5.3 shows a particle trapped at atmospheric pressure.

4.6 Electron gun

To determine the mass of the particle, we have to induce a change in its charge. This was done using an electron gun (ES40C1 Electron Source, Prevac), a device

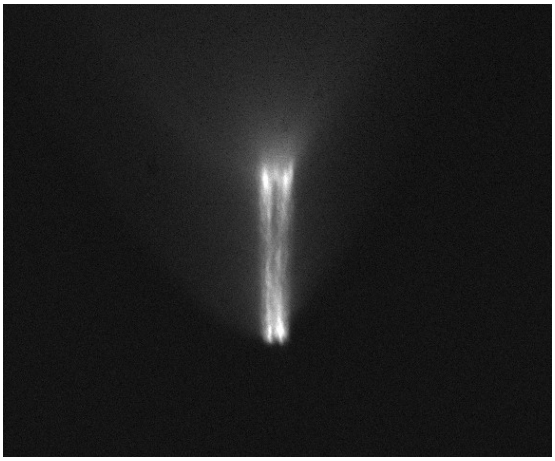

Figure 4.5.3: Trapped silica nanoparticle. In the image can be seen the Lissajous curve.

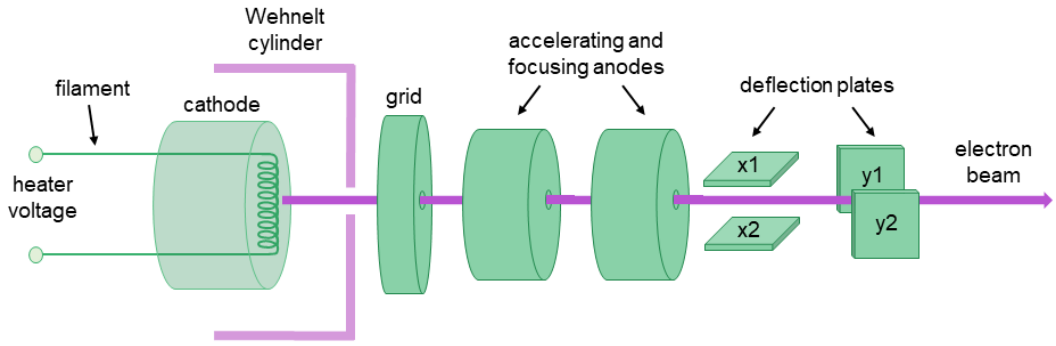

Figure 4.6.1: Diagram of an electron gun. The filament is heated up, which causes electrons to be expelled from the cathode. Then, they form into a beam when passing through a Wehnelt cylinder that has a negative charge. Afterwards, the beam is accelerated, focused and guided in a certain direction.

that works through thermionic emission. A schematic of the main parts of an e-gun is shown in figure 4.6.1.

The electron gun was controlled with a power supply device (ES40, Prevac), where we can choose the energy, emission current, focus and Wehnelt voltage. The device has a total scanning area of 10 mm $\times$ 10 mm and one can also adjust the scanning grid from 0.01 mm to 2 mm. These settings can be controlled remotely through the CODE software, and the device works only under pressures of 5×10^{-6} torr.

4.7 Cold head and cooling of the sample

To cool down the nanoparticles we use a cryocooler (CH-104 Cold head, Sumitomo) that operates with a helium compressor (HC-4A, Sumitomo). Figure 4.7.1 shows the coldhead under the vacuum chamber, although in the most recent version of the setup the coldhead is on top of the chamber. The temperature can be monitored with a controller (Model 335 Temeprature Controller, Lakeshore) that has two sensor inputs and two configurable heater outputs. This cryocooler in particular features two diode temperature sensors and a heater for temperature control.

The controller supports preloaded standard curves of temperature and also user made ones. For fine control, PID values can be set manually or with an autotuning method.

The lowest temperature we were able to reach in our first test was ∼35 K, which also contributed in lowering the pressure down to 10^{-7}. This temperature corresponds to the one detected by the sensor connected to the coldhead, whereas the sensor connected to the mount of the trap detected a temperature of ∼60 K. The temperatures we expected to attain were in the range of 20-30 K, and it can be inferred that the temperatures currently reached are higher due to the outgassing of elements inside the trap that are not optimized for high vacuum pressures.

As argon is the first species to be deposited on the surface of the nanoparticle, we have to consider its thermodynamic properties. The triple point of argon is at 83.8 K and 5.2×10^{2} torr (Gosman et al., 1969). However, for pressures of 10^{-6} torr, the solidification occurs at ∼25 K (Leming, Charles William, n.d.). Therefore, the temperature needs to be further decreased, although the value obtained is promising as an initial trial.

Figure 4.7.1: Cold head connected at the bottom of the vacuum chamber.

Chapter 5

Results and analysis

To trap a particle, we stabilize the pressure to a value in between the range of 5×10^{-3} to 9×10^{-3} torr. Then, we actuated the brush until we could see a particle on the camera or from the viewport. After this, we gradually lowered the pressure down to 10^{-6} torr, where we proceeded with the frequency monitoring and charge stepping.

To determine the secular frequencies, the Fourier transform of the particle's displacement signal was calculated. The time-averaged spectrum is presented in Figure 5.0.1.

During the first measurements, it was noticed that there was a gradual decrease in frequencies, as seen in figure 5.0.2. This could be attributed either to a gain in mass or a loss of charge. It was later deduced that this was due to the functioning of the pressure gauge. Inverted magnetron gauges work by producing electrons that collide with the background gas, ionizing the atoms positively, which can alter the charge of the trapped particle. (Frimmer et al., 2017; Redhead, 1959). This was solved by placing the gauge in a T with the electron gun, considering also the shielding from the electron gun, so the ions bombarded by the gauge wouldn't hit the particle directly.

Measurements were made where the electron gun was turned on for intervals of 25 minutes, where we could detect a change in the frequency of the particle, as shown in fig 5.0.3. Here, the minimum difference between two points of frequency data, gives us the size of the step, that is equivalent to a step of charge. The settings used for the e-gun were an energy voltage of 3400 V, emission current

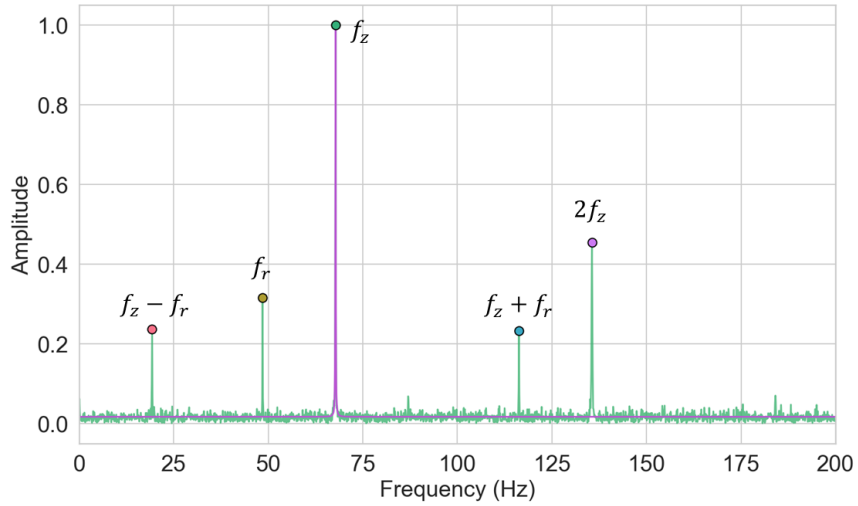

Figure 5.0.1: Secular frequencies of a SiO_2 particle at a given time, after being bombarded by the electron gun, for a trap frequency of 720 Hz and a voltage of 1549.3 Vpp. Here, $f_u = \omega_u/2\pi$. In pink, is the Lorentzian fit of f_z.

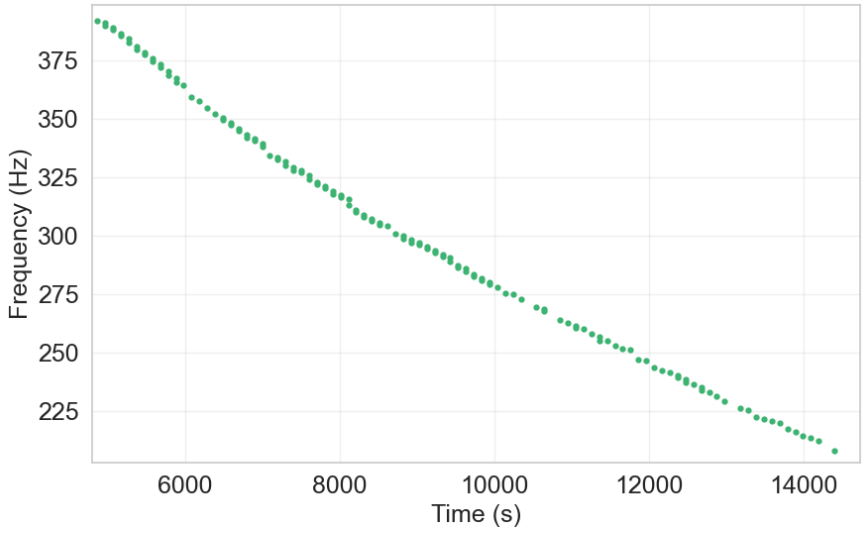

Figure 5.0.2: Monitoring of the frequency of a particle trapped at $\Omega = 2100$ Hz and $V_0 = 1420$ Vpp.

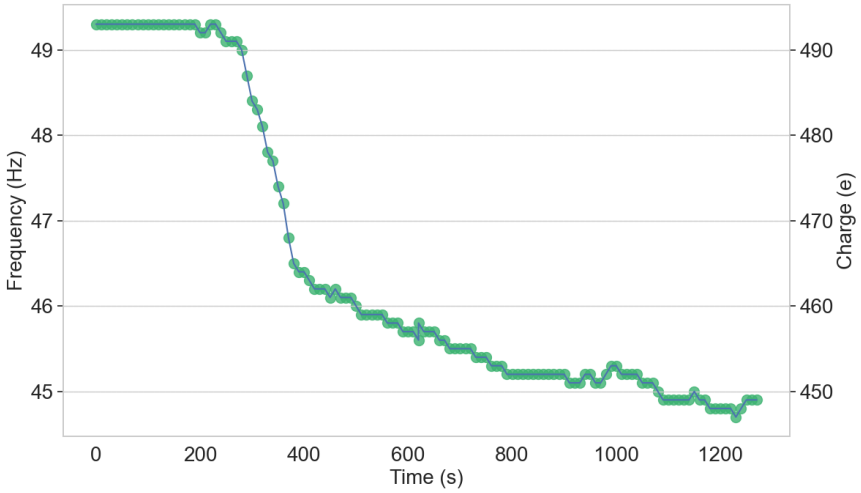

Figure 5.0.3: Axial secular frequency of a trapped particle in time while being bombarded with electrons. On the right, is shown the charge of the particle. For this data, the size of an angular frequency step is obtained to be 0.63 Hz.

of 0.10 μA, focus of 60% and Wehnelt voltage of 150 V. Regarding the trap, the frequency was 650 Hz and the voltage was of 1450 Vpp.

Now, to estimate the mass of the particle we rewrite equation 3.0.9 as

$$m = \frac{2\sqrt{2}\, eV}{\Delta\omega_z (r_0^2 + 2z_0^2)\Omega},$$

where $e = 1.602 \times 10^{-19}$ C and $\Delta\omega_z$ is the size of the step. Here, we consider that the axial frequency corresponds to the frequency with the highest amplitude in the data graphs.

From the data of figure 5.0.3, we have obtained a mass of $(4.70 \pm 0.08)\ \times 10^{-15}$ g. Since the particles used have a diameter of 160 nm, considering they are spherical, they should have a mass of $4.72\ \times 10^{-18}$ g. This number is 996 times lower than the value obtained, which means we are actually trapping a cluster of particles. It could be already seen by SEM images of the particles (figure 5.0.4) that the nanoparticles tend to clump. It was deduced that this was due to the hydroxyl layer that covers the nanoparticles (Li et al., 2024), as was mentioned in section 4.3, that makes particles stick to each other. Although this behavior can be improved by the way of drying the particles, loading them into the brush will make clumps form again.

There are a few possible solutions to this problem. One of them is increasing the

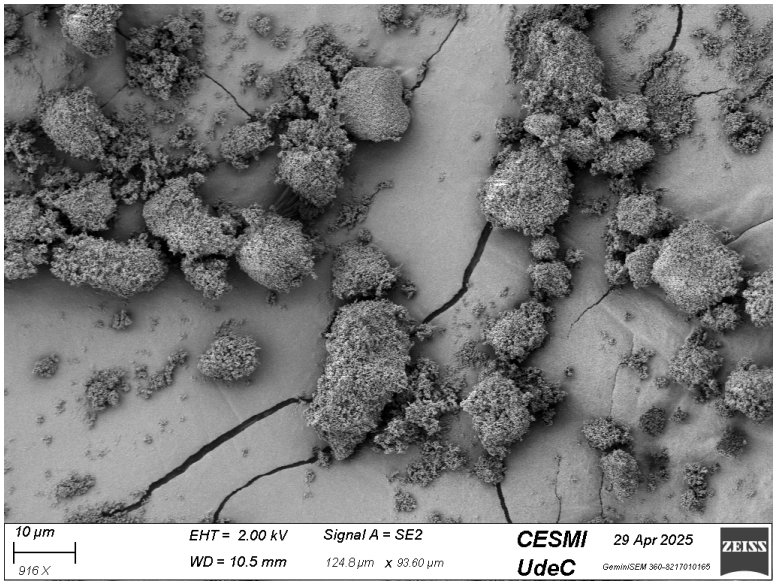

Figure 5.0.4: SEM image of the SiO_2 nanoparticles where the big clusters can be seen.

trap frequency and decreasing the voltage, so the trapping potential prioritizes smaller particles, however, these conditions have not been successful for capturing. Another solution is to synthesize bigger nanoparticles, of around 500 nm in diameter. Other ways of solving this involve changing the injection method. With the implementation of the loudspeaker, it is expected that the issue improves. In addition, new tests will be done with the ESI, since it remains as the ideal injection method for these type of experiments.

Chapter 6

Future work

The following phase of the experiment involves the cryogenic cooling of the trapped SiO_2 nanoparticles to produce the adsorption of atomic species on their surface. This can be done by detecting changes in mass that will be translated into a frequency shift. Nevertheless, there are different challenges that come with this procedure.

First is that, although we are able to measure mass with great precision, at the low pressures we are working at, the surface coverage is expected to remain in the submonolayer regime. Therefore, if the adsorbate concentration is sufficiently low, there is a chance we will not perceive the shift in mass. While it is suggested that the sensitivity of the mass spectrometer is adequate enough to detect these changes, it is still something to have into consideration.

Secondly, the accuracy of the derived adsorption isotherms is heavily dependent on the precision of local pressure measurements. It is essential to consider that the value of the equilibrium pressure used for the isotherms plot and in Henry's law, must represent the pressure directly at the gas-solid interface (Ruthven, 1984). At low concentrations, however, the isosteric method becomes increasingly sensitive to marginal errors in preassure measurement, and is not always reliable (Rouquerol et al., 2014). Knowing this with exactitude is important to determine the enthalpy of adsorption, which is equivalent to the adsorption energy. One way of determining the equilibrium pressure would be through Gay-Lussac's law

$$\frac{P_1}{T_1} = \frac{P_2}{T_2}, \tag{6.0.1}$$

where P_1 and T_1 are the pressure and temperature right by the pressure gauge, and P_2 with T_2 are the equilibrium pressure and temperature of the particle, respectively. However, this approach is currently hindered by the lack of information we have on the particle's internal temperature. This also prevents us from using other standard analytical techniques such as temperature programmed desorption. Therefore, solutions regarding pressure certainty are yet to be explored.

Establishing thermodynamic equilibrium is required for the validity of adsorption isotherms. In this experimental context, equilibrium is inferred when the secular frequency of the particle stabilizes, indicating that the rate of adsorption is equal to the rate of desorption (Rouquerol et al., 2014). We have defined the criterion for equilibrium as a constant frequency maintained over a temporal window ranging from several minutes to a couple of hours.

Furthermore, the issue of particle agglomeration, as identified in chapter 5, remains a significant variable. The transition from a single spherical nanoparticle to a clumped cluster of dozens or hundreds of particles, alters the available surface area and the potential for pore-filling effects. In such cases, the surface behaves less like an idealized smooth sphere and more like a macroporous solid. As was stated previously, this is an effect we expect to resolve in the near future to ensure the data is representative of individual cosmic dust grains.

The immediate future of CODE involves two main experimental procedures. The initial adsorption tests will be conducted using argon. Following the calibration, an RF atom source will be integrated into the system to inject species such as H and O. This configuration aims to simulate the complex grain chemistry of the ISM. By replicating the formation of ices in a controlled environment, we aim to provide fundamental data on the catalytic roles of dust surfaces in the cold regions of the universe.

Chapter 7

Conclusion

In this thesis we presented the mass spectrometry of a SiO_2 nanoparticle with high precision. By situating this work within the astrochemical context of cosmic dust evolution, we have highlighted the necessity of moving beyond bulk solid studies. While traditional surface science often relies on macroscopic samples, the research made by CODE represents a crucial step toward replicating the grains found in the cold environments of the interstellar medium.

Through a review of quadrupole ion trap theory and the application of the Mathieu equations, we provided the analytical basis required to characterize the mass to charge ratio of captured nanoparticles. The experimental part of this thesis supplied a characterization of the setup, from the vacuum system to the particle injection mechanism and their detection. The main finding of this research was the determination of the particle's mass, which was found to be significantly higher than the theoretical value for a single SiO_2 nanoparticle of a 160 nm diameter. This result provides insight into the challenges of nanoparticle isolation. It suggests the presence of particle agglomeration, phenomena that must be controlled to achieve the single grain precision required for future binding energy experiments.

The methodologies explored here for determining binding energies between adsorbates and surfaces lay the groundwork for the next phase of the CODE project. By addressing the identified challenges, it is expected that future iterations of this experiment will be able to measure surface interactions with high sensitivity.

Ultimately, the transition from bulk observations to the study of individual, levitated grains will allow for a more accurate determination of how molecules

form on dust surfaces in space.

Bibliography

Almeida, R. M., & Pantano, C. G. (1990). Structural investigation of silica gel films by infrared spectroscopy. *Journal of Applied Physics*, *68*(8), 4225–4232. https://doi.org/10.1063/1.346213

An, S. S. A., Kim, K.-M., Kim, H. M., Lee, W.-J., Lee, C.-W., Kim, T.-i., Lee, J.-K., Jeong, J., Paek, S.-M., & Shin, J.-H. (2014). Surface treatment of silica nanoparticles for stable and charge-controlled colloidal silica. *International Journal of Nanomedicine*, 29. https://doi.org/10.2147/IJN.S57922

Anderson, J. (1994). A Comparison of Experimental Data and Model Predictions for Tribocharging of Two-Component Electrophotographic Developers. *Journal of Imaging Science and Technology*, *38*, 378–382.

Antczak, G., & Ehrlich, G. (2007). Jump processes in surface diffusion. *Surface Science Reports*, *62*(2), 39–61. https://doi.org/10.1016/j.surfrep.2006.12.001

Atkins, P. W., De Paula, J., & Keeler, J. (2023). *Atkins' physical chemistry* (Twelfth edition). Oxford University Press.

Batzill, M., & Diebold, U. (2005). The surface and materials science of tin oxide. *Progress in Surface Science*, *79*(2–4), 47–154. https://doi.org/10.1016/j.progsurf.2005.09.002

Baxter, R. J., & Hu, P. (2002). Insight into why the Langmuir–Hinshelwood mechanism is generally preferred. *The Journal of Chemical Physics*, *116*(11), 4379–4381. https://doi.org/10.1063/1.1458938

Bernet, T., Canu, C., & Jackson, G. (2026). Revisiting the Classification of Physisorption Isotherms with Classical Density Functional Theory. *The Journal of Physical Chemistry B*, *130*(6), 1933–1949. https://doi.org/10.1021/acs.jpcb.5c08129

Brunauer, S., Deming, L. S., Deming, W. E., & Teller, E. (1940). On a Theory of the van der Waals Adsorption of Gases. *Journal of the American Chemical Society*, *62*(7), 1723–1732. https://doi.org/10.1021/ja01864a025

Brunauer, S., Emmett, P. H., & Teller, E. (1938). Adsorption of Gases in Multimolecular Layers. *Journal of the American Chemical Society*, *60*(2), 309–319. https://doi.org/10.1021/ja01269a023

Burke, D. J., & Brown, W. A. (2010). Ice in space: Surface science investigations of the thermal desorption of model interstellar ices on dust grain analogue surfaces. *Physical Chemistry Chemical Physics*, *12*(23), 5947. https://doi.org/10.1039/b917005g

Castle, G., & Schein, L. (1995). General model of sphere-sphere insulator contact electrification. *Journal of Electrostatics*, *36*(2), 165–173. https://doi.org/10.1016/0304-3886(95)00043-7

Cheng, Z., Shan, H., Sun, Y., Zhang, L., Jiang, H., & Li, C. (2020). Evolution mechanism of surface hydroxyl groups of silica during heat treatment. *Applied Surface Science*, *513*, 145766. https://doi.org/10.1016/j.apsusc.2020.145766

Cui, W., & Herbst, E. (2024). Exploring the Role of Ion–Molecule Reactions on Interstellar Icy Grain Surfaces. *ACS Earth and Space Chemistry*, *8*(11), 2218–2231. https://doi.org/10.1021/acsearthspacechem.4c00194

Cuppen, H. M., Walsh, C., Lamberts, T., Semenov, D., Garrod, R. T., Penteado, E. M., & Ioppolo, S. (2017). Grain Surface Models and Data for Astrochemistry. *Space Science Reviews*, *212*(1–2), 1–58. https://doi.org/10.1007/s11214-016-0319-3

Dąbrowski, A. (2001). Adsorption — from theory to practice. *Advances in Colloid and Interface Science*, *93*(1–3), 135–224. https://doi.org/10.1016/S0001-8686(00)00082-8

Donohue, M., & Aranovich, G. (1999). A new classification of isotherms for Gibbs adsorption of gases on solids. *Fluid Phase Equilibria*, *158–160*, 557–563. https://doi.org/10.1016/S0378-3812(99)00074-6

Draine, B. T. (2003a). Interstellar Dust Grains. https://doi.org/10.48550/ARXIV.ASTRO-PH/0304489

Draine, B. T. (2003b, April 28). *Astrophysics of Dust in Cold Clouds*. arXiv: astro-ph/0304488. https://doi.org/10.48550/arXiv.astro-ph/0304488

Draine, B. T. (2009). *Interstellar Dust Models and Evolutionary Implications* (1). https://doi.org/10.48550/ARXIV.0903.1658

Dulieu, F., Amiaud, L., Congiu, E., Fillion, J.-H., Matar, E., Momeni, A., Pirronello, V., & Lemaire, J. L. (2010). Experimental evidence for water formation on interstellar dust grains by hydrogen and oxygen atoms. *Astronomy and Astrophysics*, *512*, A30. https://doi.org/10.1051/0004-6361/200912079

Esser, T. K., Hoffmann, B., Anderson, S. L., & Asmis, K. R. (2019). A cryogenic single nanoparticle action spectrometer. *Review of Scientific Instruments*, *90*(12), 125110. https://doi.org/10.1063/1.5128203

Fraser, H. J., Collings, M. P., & McCoustra, M. R. S. (2002). Laboratory surface astrophysics experiment. *Review of Scientific Instruments*, *73*(5), 2161–2170. https://doi.org/10.1063/1.1470232

Frimmer, M., Luszcz, K., Ferreiro, S., Jain, V., Hebestreit, E., & Novotny, L. (2017). Controlling the net charge on a nanoparticle optically levitated in vacuum. *Physical Review A*, *95*(6), 061801. https://doi.org/10.1103/PhysRevA.95.061801

Gerlich, D., & Decker, S. (2014). Trapping ions at high temperatures: Thermal decay of C60 +. *Applied Physics B*, *114*(1–2), 257–266. https://doi.org/10.1007/s00340-013-5668-y

Gilliland, E. R., Baddour, R. F., Perkinson, G. P., & Sladek, K. J. (1974). Diffusion on Surfaces. I. Effect of Concentration on the Diffusivity of Physically Adsorbed Gases. *Industrial & Engineering Chemistry Fundamentals*, *13*(2), 95–100. https://doi.org/10.1021/i160050a001

Gosman, A. L., McCarty, R. D., & Hust, J. G. (1969). *Thermodynamic properties of argon from the triple point to 300 K at pressures to 1000 atmospheres* (0th ed., NBS NSRDS 27). National Bureau of Standards. Gaithersburg, MD. https://doi.org/10.6028/NBS.NSRDS.27

Gouveia, R. F., Costa, C. A. R., & Galembeck, F. (2008). Water Vapor Adsorption Effect on Silica Surface Electrostatic Patterning. *The Journal of Physical Chemistry C*, *112*(44), 17193–17199. https://doi.org/10.1021/jp803812p

Green, S. D., Bolina, A. S., Chen, R., Collings, M. P., Brown, W. A., & McCoustra, M. R. S. (2009). Applying laboratory thermal desorption data in an interstellar context: Sublimation of methanol thin films. *Monthly Notices of the Royal Astronomical Society*, *398*(1), 357–367. https://doi.org/10.1111/j.1365-2966.2009.15144.x

Grimm, M., Langer, B., Schlemmer, S., Lischke, T., Becker, U., Widdra, W., Gerlich, D., Flesch, R., & Rühl, E. (2006). Charging Mechanisms of Trapped Element-Selectively Excited Nanoparticles Exposed to Soft X Rays. *Physical Review Letters*, *96*(6), 066801. https://doi.org/10.1103/PhysRevLett.96.066801

Guélin, M., & Cernicharo, J. (2022). Organic Molecules in Interstellar Space: Latest Advances. *Frontiers in Astronomy and Space Sciences*, *9*, 787567. https://doi.org/10.3389/fspas.2022.787567

Hama, T., & Watanabe, N. (2013). Surface Processes on Interstellar Amorphous Solid Water: Adsorption, Diffusion, Tunneling Reactions, and Nuclear-Spin Conversion. *Chemical Reviews*, *113*(12), 8783–8839. https://doi.org/10.1021/cr4000978

Henning, T. (2010). Cosmic Silicates. *Annual Review of Astronomy and Astrophysics*, *48*(1), 21–46. https://doi.org/10.1146/annurev-astro-081309-130815

Herbst, E. (2005). Chemistry of Star-Forming Regions. *The Journal of Physical Chemistry A*, *109*(18), 4017–4029. https://doi.org/10.1021/jp050461c

Herbst, E., & Van Dishoeck, E. F. (2009). Complex Organic Interstellar Molecules. *Annual Review of Astronomy and Astrophysics*, *47*(1), 427–480. https://doi.org/10.1146/annurev-astro-082708-101654

Hill, C. G. (1977). *An introduction to chemical engineering kinetics & reactor design*. Wiley.

Ho, C. S., Lam, C. W. K., Chan, M. H. M., Cheung, R. C. K., Law, L. K., Lit, L. C. W., Ng, K. F., Suen, M. W. M., & Tai, H. L. (2003). Electrospray ionisation mass spectrometry: Principles and clinical applications. *The Clinical Biochemist. Reviews*, *24*(1), 3–12.

Howder, C. R., Bell, D. M., & Anderson, S. L. (2014). Optically detected, single nanoparticle mass spectrometer with pre-filtered electrospray nanoparticle

source. *Review of Scientific Instruments*, *85*(1), 014104. https://doi.org/10.1063/1.4861923

Ibach, H. (2006). *Physics of Surfaces and Interfaces*. Springer Berlin Heidelberg. https://doi.org/10.1007/3-540-34710-0

Ifergane, S., David, R. B., Sabatani, E., Carmeli, B., Beeri, O., & Eliaz, N. (2018). Hydrogen Diffusivity and Trapping in Custom 465 Stainless Steel. *Journal of The Electrochemical Society*, *165*(3), C107–C115. https://doi.org/10.1149/2.0261803jes

Kebarle, P., & Verkerk, U. H. (2009). Electrospray: From ions in solution to ions in the gas phase, what we know now. *Mass Spectrometry Reviews*, *28*(6), 898–917. https://doi.org/10.1002/mas.20247

Kemper, F., Vriend, W. J., & Tielens, A. G. G. M. (2004). The Absence of Crystalline Silicates in the Diffuse Interstellar Medium. *The Astrophysical Journal*, *609*(2), 826–837. https://doi.org/10.1086/421339

Kiani, D., & Wachs, I. E. (2024). Practical Considerations for Understanding Surface Reaction Mechanisms Involved in Heterogeneous Catalysis. *ACS Catalysis*, *14*(22), 16770–16784. https://doi.org/10.1021/acscatal.4c05188

Kim, T. G., An, G. S., Han, J. S., Hur, J. U., Park, B. G., & Choi, S.-C. (2017). Synthesis of Size Controlled Spherical Silica Nanoparticles via Sol-Gel Process within Hydrophilic Solvent. *Journal of the Korean Ceramic Society*, *54*(1), 49–54. https://doi.org/10.4191/kcers.2017.54.1.10

Kim, Y. J., Lee, J., Park, S., Park, C., Park, C., & Choi, H.-J. (2017). Effect of the relative permittivity of oxides on the performance of triboelectric nanogenerators. *RSC Adv.*, *7*(78), 49368–49373. https://doi.org/10.1039/C7RA07274K

Klessen, R. S., & Glover, S. C. O. (2014). *Physical Processes in the Interstellar Medium* (1). https://doi.org/10.48550/ARXIV.1412.5182

Konermann, L., Ahadi, E., Rodriguez, A. D., & Vahidi, S. (2013). Unraveling the Mechanism of Electrospray Ionization. *Analytical Chemistry*, *85*(1), 2–9. https://doi.org/10.1021/ac302789c

Krasnokutski, S. A., Rouillé, G., Jäger, C., Huisken, F., Zhukovska, S., & Henning, Th. (2014). FORMATION OF SILICON OXIDE GRAINS AT LOW TEMPERATURE. *The Astrophysical Journal*, *782*(1), 15. https://doi.org/10.1088/0004-637X/782/1/15

Lacks, D. J., & Shinbrot, T. (2019). Long-standing and unresolved issues in triboelectric charging. *Nature Reviews Chemistry*, *3*(8), 465–476. https://doi.org/10.1038/s41570-019-0115-1

Langmuir, I. (1918). THE ADSORPTION OF GASES ON PLANE SURFACES OF GLASS, MICA AND PLATINUM. *Journal of the American Chemical Society*, *40*(9), 1361–1403. https://doi.org/10.1021/ja02242a004

Le Bourlot, J., Le Petit, F., Pinto, C., Roueff, E., & Roy, F. (2012). Surface chemistry in the interstellar medium: I. H_2 formation by Langmuir-Hinshelwood and Eley-Rideal mechanisms. *Astronomy & Astrophysics*, *541*, A76. https://doi.org/10.1051/0004-6361/201118126

Lee, V., James, N. M., Waitukaitis, S. R., & Jaeger, H. M. (2018). Collisional charging of individual submillimeter particles: Using ultrasonic levitation to initiate and track charge transfer. *Physical Review Materials*, *2*(3), 035602. https://doi.org/10.1103/PhysRevMaterials.2.035602

Leming, Charles William. (n.d.). *Sublimation pressures of solid argon, krypton and xenon*. https://doi.org/10.25335/SCWC-ES24

Lennard-Jones, J. E. (1932). Processes of adsorption and diffusion on solid surfaces. *Transactions of the Faraday Society*, *28*, 333. https://doi.org/10.1039/tf9322800333

Li, C., Ma, Y., Wang, J., Ying, Q., Zhu, S., Fu, Z., Jiang, X., Yang, H., Liang, T., Gao, X., & Hu, H. (2024). Morphological Tracking and Tuning of Silica Nanoparticles in Optomechanical Systems for Enhanced Stable Levitation in Vacuum. *ACS Applied Nano Materials*, *7*(22), 25493–25499. https://doi.org/10.1021/acsanm.4c04437

Linnartz, H., Ioppolo, S., & Fedoseev, G. (2015). Atom addition reactions in interstellar ice analogues. *International Reviews in Physical Chemistry*, *34*(2), 205–237. https://doi.org/10.1080/0144235X.2015.1046679

Liuni, P., & Wilson, D. J. (2011). Understanding and optimizing electrospray ionization techniques for proteomic analysis. *Expert Review of Proteomics*, *8*(2), 197–209. https://doi.org/10.1586/epr.10.111

Lüth, H. (2015). *Solid Surfaces, Interfaces and Thin Films*. Springer International Publishing. https://doi.org/10.1007/978-3-319-10756-1

Magdy, A., Mostafa, M. R., Moustafa, S. A., Mohamed, G. G., & Fouad, O. A. (2024). Kinetics and adsorption isotherms studies for the effective removal of Evans blue dye from an aqueous solution utilizing forsterite nanoparticles. *Scientific Reports*, *14*(1), 24392. https://doi.org/10.1038/s41598-024-73697-x

March, R. E., & Todd, J. F. J. (2005, August 5). *Quadrupole Ion Trap Mass Spectrometry* (1st ed.). Wiley. https://doi.org/10.1002/0471717983

Martínez Sepúlveda, N., Moena Ilijić, F., Condeza, C., Solano, P., & Bovino, S. (2026). The cosmic dust experiment: A nanoparticle non-destructive mass spectrometer for astrochemical studies. *The European Physical Journal Plus*, *141*(5), 531. https://doi.org/10.1140/epjp/s13360-026-07746-x

Matsusaka, S., Maruyama, H., Matsuyama, T., & Ghadiri, M. (2010). Triboelectric charging of powders: A review. *Chemical Engineering Science*, *65*(22), 5781–5807. https://doi.org/10.1016/j.ces.2010.07.005

Medveď, I., & Černý, R. (2011). Surface diffusion in porous media: A critical review. *Microporous and Mesoporous Materials*, *142*(2–3), 405–422. https://doi.org/10.1016/j.micromeso.2011.01.015

Min, M., Waters, L. B. F. M., De Koter, A., Hovenier, J. W., Keller, L. P., & Markwick-Kemper, F. (2007). The shape and composition of interstellar silicate grains. *Astronomy & Astrophysics*, *462*(2), 667–676. https://doi.org/10.1051/0004-6361:20065436

Naumovets, A., & Vedula, Y. (1985). Surface diffusion of adsorbates. *Surface Science Reports*, *4*(7–8), 365–434. https://doi.org/10.1016/0167-5729(85)90007-X

Noble, J. A., Congiu, E., Dulieu, F., & Fraser, H. J. (2012). Thermal desorption characteristics of CO, O2 and CO2 on non-porous water, crystalline water and silicate surfaces at submonolayer and multilayer coverages: Desorption from H2O(np), H2O(c) and SiOx. *Monthly Notices of the Royal Astronomical Society*, no–no. https://doi.org/10.1111/j.1365-2966.2011.20351.x

Pan, S., & Zhang, Z. (2019). Fundamental theories and basic principles of triboelectric effect: A review. *Friction*, *7*(1), 2–17. https://doi.org/10.1007/s40544-018-0217-7

Paparazzo, E., Fanfoni, M., Severini, E., & Priori, S. (1992). Evidence of Si–OH species at the surface of aged silica. *Journal of Vacuum Science & Technology A: Vacuum, Surfaces, and Films*, *10*(4), 2892–2896. https://doi.org/10.1116/1.577726

Peng, L., Qisui, W., Xi, L., & Chaocan, Z. (2009). Investigation of the states of water and OH groups on the surface of silica. *Colloids and Surfaces A: Physicochemical and Engineering Aspects*, *334*(1–3), 112–115. https://doi.org/10.1016/j.colsurfa.2008.10.028

Potapov, A., Jäger, C., & Henning, T. (2020). Ice Coverage of Dust Grains in Cold Astrophysical Environments. *Physical Review Letters*, *124*(22), 221103. https://doi.org/10.1103/PhysRevLett.124.221103

Potapov, A., & McCoustra, M. (2021). Physics and chemistry on the surface of cosmic dust grains: A laboratory view. *International Reviews in Physical Chemistry*, *40*(2), 299–364. https://doi.org/10.1080/0144235X.2021.1918498

Prins, R. (2018). Eley–Rideal, the Other Mechanism. *Topics in Catalysis*, *61*(9–11), 714–721. https://doi.org/10.1007/s11244-018-0948-8

Rahman, I. A., & Padavettan, V. (2012). Synthesis of Silica Nanoparticles by Sol-Gel: Size-Dependent Properties, Surface Modification, and Applications in Silica-Polymer Nanocomposites—A Review (S. P. Davtyan, Ed.). *Journal of Nanomaterials*, *2012*(1), 132424. https://doi.org/10.1155/2012/132424

Redhead, P. A. (1959). THE MAGNETRON GAUGE: A COLD-CATHODE VACUUM GAUGE. *Canadian Journal of Physics*, *37*(11), 1260–1271. https://doi.org/10.1139/p59-144

Redhead, P. (1962). Thermal desorption of gases. *Vacuum*, *12*(4), 203–211. https://doi.org/10.1016/0042-207X(62)90978-8

Roles, J., & Guiochon, G. (1992). Experimental determination of adsorption isotherm data for the study of the surface energy distribution of various solid surfaces by inverse gas-solid chromatography. *Journal of Chromatography A*, *591*(1–2), 233–243. https://doi.org/10.1016/0021-9673(92)80242-M

Rouquerol, F., Rouquerol, J., Sing, K. S. W., Llewellyn, P. L., & Maurin, G. (2014). *Adsorption by powders and porous solids: Principles, methodology and applications* (Second edition). Elsevier/AP.

Ruthven, D. M. (1984). *Principles of adsorption and adsorption processes*. Wiley.

Schlemmer, S., Wellert, S., Windisch, F., Grimm, M., Barth, S., & Gerlich, D. (2004). Interaction of electrons and molecules with a single trapped nanoparticle. *Applied Physics A: Materials Science & Processing*, *78*(5), 629–636. https://doi.org/10.1007/s00339-003-2270-x

Schlemmer, S., Illemann, J., Wellert, S., & Gerlich, D. (1999). Non-destructive, absolute mass determination of sub-micrometer sized particles in a Paul-type trap, 80–86. https://doi.org/10.1063/1.57485

Schlemmer, S., Illemann, J., Wellert, S., & Gerlich, D. (2001). Nondestructive high-resolution and absolute mass determination of single charged particles in a three-dimensional quadrupole trap. *Journal of Applied Physics*, *90*(10), 5410–5418. https://doi.org/10.1063/1.1397295

Schmid, M., Parkinson, G. S., & Diebold, U. (2023). Analysis of Temperature-Programmed Desorption via Equilibrium Thermodynamics. *ACS Physical Chemistry Au*, *3*(1), 44–62. https://doi.org/10.1021/acsphyschemau.2c00031

Sepsey, A. (2022). An Adventurous Journey Around the Thermodynamics of Liquid Chromatography. *LCGC North America*, 584–586. https://doi.org/10.56530/lcgc.na.qk2090y9

Shaw, P. E., & Jex, C. S. (1928). Tribo-electricity and friction. II.—Glass and solid elements. *Proceedings of the Royal Society of London. Series A, Containing Papers of a Mathematical and Physical Character*, *118*(779), 97–108. https://doi.org/10.1098/rspa.1928.0037

Sing, K. S. W. (1985). Reporting physisorption data for gas/solid systems with special reference to the determination of surface area and porosity (Recommendations 1984). *Pure and Applied Chemistry*, *57*(4), 603–619. https://doi.org/10.1351/pac198557040603

Snow, T. P., & McCall, B. J. (2006). Diffuse Atomic and Molecular Clouds. *Annual Review of Astronomy and Astrophysics*, *44*(1), 367–414. https://doi.org/10.1146/annurev.astro.43.072103.150624

Stöber, W., Fink, A., & Bohn, E. (1968). Controlled growth of monodisperse silica spheres in the micron size range. *Journal of Colloid and Interface Science*, *26*(1), 62–69. https://doi.org/10.1016/0021-9797(68)90272-5

Studemund, T., Pollow, K., Förstel, M., Mickein, E., Breier, A. A., & Dopfer, O. (2025). Optical Spectroscopy and Photochemistry of Silicon Oxide Cations: The Case of Triatomic Si_2 O^+ and $SiO_2{}^+$. *ACS Earth and Space Chemistry*, *9*(1), 178–190. https://doi.org/10.1021/acsearthspacechem.4c00326

Swenson, H., & Stadie, N. P. (2019). Langmuir's Theory of Adsorption: A Centennial Review. *Langmuir*, *35*(16), 5409–5426. https://doi.org/10.1021/acs.langmuir.9b00154

Thommes, M., Kaneko, K., Neimark, A. V., Olivier, J. P., Rodriguez-Reinoso, F., Rouquerol, J., & Sing, K. S. (2015). Physisorption of gases, with special reference to the evaluation of surface area and pore size distribution (IUPAC Technical Report). *Pure and Applied Chemistry*, *87*(9–10), 1051–1069. https://doi.org/10.1515/pac-2014-1117

Tielens, A. G. G. M. (2013). The molecular universe. *Reviews of Modern Physics*, *85*(3), 1021–1081. https://doi.org/10.1103/RevModPhys.85.1021

Vidali, G. (2013). H_2 Formation on Interstellar Grains. *Chemical Reviews*, *113*(12), 8762–8782. https://doi.org/10.1021/cr400156b

Wakelam, V., Bron, E., Cazaux, S., Dulieu, F., Gry, C., Guillard, P., Habart, E., Hornekær, L., Morisset, S., Nyman, G., Pirronello, V., Price, S. D., Valdivia, V., Vidali, G., & Watanabe, N. (2017). H 2 formation on interstellar dust grains: The viewpoints of theory, experiments, models and observations. *Molecular Astrophysics*, *9*, 1–36. https://doi.org/10.1016/j.molap.2017.11.001

Wiese, H. (1991). A. W. Adamson: "Physical Chemistry of Surfaces", 5. Auflage, John Wiley & Sons Inc., New York, Chichester, Brisbane, Toronto, Singapore 1990. 777 Seiten, Preis: £ 47.50. *Berichte der Bunsengesellschaft für physikalische Chemie*, *95*(6), 758–758. https://doi.org/10.1002/bbpc.19910950629

Yamamoto, S. (2017). *Introduction to Astrochemistry*. Springer Japan. https://doi.org/10.1007/978-4-431-54171-4